

Disabling Uncompetitive Inhibition of Oncogenic IDH Mutations Drives Acquired Resistance



Junhua Lyu^{1,2}, Yuxuan Liu^{1,2}, Lihu Gong³, Mingyi Chen⁴, Yazan F. Madanat⁵, Yuannu Zhang^{1,2}, Feng Cai¹, Zhimin Gu^{1,2}, Hui Cao^{1,2}, Pranita Kaphle^{1,2}, Yoon Jung Kim^{1,2}, Fatma N. Kalkan⁵, Helen Stephens⁵, Kathryn E. Dickerson^{1,2}, Min Ni¹, Weina Chen⁴, Prapti Patel⁵, Alice S. Mims⁶, Uma Borate⁷, Amy Burd⁸, Sheng F. Cai⁹, C. Cameron Yin¹⁰, M. James You¹⁰, Stephen S. Chung⁵, Robert H. Collins⁵, Ralph J. DeBerardinis^{1,11}, Xin Liu³, and Jian Xu^{1,2}



ABSTRACT

Mutations in IDH genes occur frequently in acute myeloid leukemia (AML) and other human cancers to generate the oncometabolite *R*-2HG. Allosteric inhibition of mutant IDH suppresses *R*-2HG production in a subset of patients with AML; however, acquired resistance emerges as a new challenge, and the underlying mechanisms remain incompletely understood. Here we establish isogenic leukemia cells containing common IDH oncogenic mutations by CRISPR base editing. By mutational scanning of IDH single amino acid variants in base-edited cells, we describe a repertoire of IDH second-site mutations responsible for therapy resistance through disabling uncompetitive enzyme inhibition. Recurrent mutations at NADPH binding sites within IDH heterodimers act in *cis* or *trans* to prevent the formation of stable enzyme-inhibitor complexes, restore *R*-2HG production in the presence of inhibitors, and drive therapy resistance in IDH-mutant AML cells and patients. We therefore uncover a new class of pathogenic mutations and mechanisms for acquired resistance to targeted cancer therapies.

SIGNIFICANCE: Comprehensive scanning of IDH single amino acid variants in base-edited leukemia cells uncovers recurrent mutations conferring resistance to IDH inhibition through disabling NADPH-dependent uncompetitive inhibition. Together with targeted sequencing, structural, and functional studies, we identify a new class of pathogenic mutations and mechanisms for acquired resistance to IDH-targeting cancer therapies.

INTRODUCTION

Cytosolic isocitrate dehydrogenase (IDH) 1 and mitochondrial IDH2 catalyze the oxidative decarboxylation of isocitrate (ICT) to α -ketoglutarate (α KG) with the concomitant production of nicotinamide adenine dinucleotide phosphate (NADPH). Somatic mutations in the catalytic arginine residues of IDH occur frequently in acute myeloid leukemia (AML) and other cancers (1–3) through gain-of-function activity by catalyzing NADPH-dependent α KG reduction to

the oncometabolite (*R*)-2-hydroxyglutarate (*R*-2HG, or 2HG; refs. 4–6). Accumulating *R*-2HG causes altered histone and DNA methylation by impairing α KG-dependent dioxygenases (7–10). Allosteric inhibitors of mutant IDH suppress *R*-2HG production and induce differentiation of leukemic blasts, providing clinical responses in approximately 40% of treated AML patients with mutant IDH (11–13). These findings provide the basis of targeted therapies for AML (ivosidenib and enasidenib), establishing the first example of personalized therapy based on cancer metabolism. However, the development of treatment resistance to IDH inhibitors emerges as a new challenge. Most patients who initially responded eventually relapsed, whereas a thorough analysis of the mutational landscape and mechanisms for acquired resistance to IDH inhibition has been difficult.

Small-molecule inhibitors comprise about half of cancer-targeting drugs, which commonly involve the competitive, noncompetitive, or uncompetitive mechanism of inhibition (14). Competitive inhibitors resemble the normal substrates and thus prevent substrate binding to the enzymes, whereas noncompetitive inhibitors bind equally well to the enzyme and the enzyme-substrate complexes to impact enzymatic activity. By contrast, uncompetitive inhibitors bind only to the complex formed between the enzyme and the substrate, thus requiring the formation of a stable enzyme-substrate complex prior to inhibitor binding. It remains elusive whether and how the unique biochemical features of IDH inhibitors contribute to the development of clinical resistance.

Studies of small cohorts revealed a subset of acquired mutations at the IDH dimer interface that restore *R*-2HG production by interference with allosteric inhibitor binding (15). The emergence of mutations in the IDH homolog during the inhibition of the other mutant IDH protein, or isoform switching, also contributes to resistance by *R*-2HG restoration (16). These findings underscore a pivotal role for maintaining *R*-2HG production in IDH-mutant (IDH^{mut})

¹Children's Medical Center Research Institute, University of Texas Southwestern Medical Center, Dallas, Texas. ²Department of Pediatrics, Harold C. Simmons Comprehensive Cancer Center, and Hamon Center for Regenerative Science and Medicine, University of Texas Southwestern Medical Center, Dallas, Texas. ³Cecil H. and Ida Green Center for Reproductive Biology Sciences, Department of Obstetrics and Gynecology, and Department of Biophysics, University of Texas Southwestern Medical Center, Dallas, Texas. ⁴Department of Pathology, University of Texas Southwestern Medical Center, Dallas, Texas. ⁵Department of Internal Medicine, University of Texas Southwestern Medical Center, Dallas, Texas. ⁶Division of Hematology, Department of Internal Medicine, The Ohio State University Comprehensive Cancer Center, Columbus, Ohio. ⁷Division of Hematology and Medical Oncology, Department of Medicine, Oregon Health and Science University, Portland, Oregon. ⁸The Leukemia & Lymphoma Society, Rye Brook, New York. ⁹Leukemia Service, Department of Medicine, Memorial Sloan Kettering Cancer Center, New York, New York. ¹⁰Department of Hematopathology, The University of Texas MD Anderson Cancer Center, Houston, Texas. ¹¹Howard Hughes Medical Institute, University of Texas Southwestern Medical Center, Dallas, Texas.

Corresponding Author: Jian Xu, Children's Medical Center Research Institute, University of Texas Southwestern Medical Center, 6000 Harry Hines Boulevard, Dallas, TX 75235. Phone: 214-648-6125; E-mail: jian.xu@utsouthwestern.edu

Cancer Discov 2023;13:170-93

doi: 10.1158/2159-8290.CD-21-1661

This open access article is distributed under the Creative Commons Attribution-NonCommercial-NoDerivatives 4.0 International (CC BY-NC-ND 4.0) license.

©2022 The Authors; Published by the American Association for Cancer Research

malignancies and establish R-2HG–restoring mutations as a crucial mechanism in therapy resistance. Although mutations conferring resistance to IDH inhibition are increasingly identified (17, 18), the entire repertoire of IDH second-site mutations with the potential to induce therapy resistance has not been systematically evaluated. Moreover, our understanding of the mechanisms for R-2HG–restoring mutations remains incomplete. This is due in large part to the lack of preclinical cell models and an unbiased analysis of clinically relevant IDH second-site mutations.

Here we developed a panel of isogenic leukemia cell lines containing the most common *IDH1* or *IDH2* oncogenic mutations by CRISPR base editing. We performed saturation mutagenesis screens of IDH single amino acid variants and identified second-site mutations conferring resistance to IDH inhibition in base-edited leukemia cells. We integrated these results with targeted sequencing of patients with AML, structural modeling, enzymology, and functional validation in humanized mouse models. Our findings not only validate known mutations associated with resistance to IDH inhibition but also uncover a new class of pathogenic mutations and the underlying mechanisms for resistance to IDH-targeting cancer therapies.

RESULTS

Generation of Base-Edited *IDH^{mut}* Leukemia Cells

To survey the prevalence of R-2HG–restoring mutations in human AML, we evaluated 31 relapsed or refractory *IDH^{mut}* AML cases previously described to have sustained R-2HG despite treatment with mutant IDH1 or IDH2 inhibitors (15–19). We identified 16 of 31 (or 51.6%) cases of isoform switching, 13 of 31 (41.9%) cases of second-site mutations, and 2 of 31 (6.5%) cases of both mutation types (Fig. 1A; Supplementary Table S1). Importantly, among the IDH second-site mutations, 40% (6 of 15) are known to affect the allosteric binding of *IDH^{mut}* inhibitors to the dimer interface including *IDH1^{S280F}*, *IDH2^{Q316E}*, and *IDH2^{I319M}* (15), whereas the mechanisms for the other mutations are unknown (Fig. 1A), illustrating a deficiency in our current understanding of therapy resistance to IDH inhibition.

Due to the lack of leukemia cell models harboring endogenous IDH mutations, prior studies of mutant IDH have relied on overexpressing *IDH^{mut}* proteins in cells with wild-type *IDH1* and *IDH2* genes (20–22), which may not fully recapitulate the molecular events and therapy response driven by mutant IDH. To address this, we used CRISPR base editing to engineer clinically relevant isogenic cell models with monoallelic *IDH1* or *IDH2* mutations. The GM-CSF-dependent human TF-1 erythroleukemia cells were previously used as a model to evaluate the biological function and allosteric inhibition of *IDH^{mut}* proteins (12, 22, 23). We used the optimized CRISPR base editor (Cas9-BE) with the fusion of Cas9n (Cas9^{D10A}), cytidine deaminase, and a uracil glycosylase inhibitor (UGI) to introduce C:G-to-T:A transitions (24, 25) using single-guide RNAs (sgRNA) designed to target individual *IDH* hotspot mutations including *IDH1^{R132H}*, *IDH2^{R140Q}*, *IDH2^{R140W}*, and *IDH2^{R172K}*, respectively (Fig. 1B; Supplementary Fig. S1A). Upon base editing, we screened single cell-derived clonal

lines and confirmed monoallelic *IDH1^{WT/mut}* or *IDH2^{WT/mut}* genotypes by targeted sequencing of genomic DNA (Supplementary Fig. S1B; Supplementary Table S2).

To assess the functional impact of base-edited *IDH^{mut}* genes in leukemia cells, we first determined R-2HG levels by mass spectrometry in the representative *IDH1^{R132H}* (clone D5, hereafter *IDH1^{R132H}-BE*) and *IDH2^{R140Q}* (clone B4, hereafter *IDH2^{R140Q}-BE*) cells. Compared with unedited parental TF-1 cells, R-2HG levels were significantly increased in the pellets and medium of *IDH1^{R132H}-BE* and *IDH2^{R140Q}-BE* cells, similar to that observed in TF-1 cells stably overexpressing *IDH1^{R132H}* or *IDH2^{R140Q}* (hereafter *IDH1^{R132H}-OE* and *IDH2^{R140Q}-OE*; Fig. 1C), illustrating the gain-of-function activity of base-edited *IDH^{mut}* proteins. Moreover, *IDH1^{R132H}-BE* and *IDH2^{R140Q}-BE* cells acquired GM-CSF cytokine-independent cell growth and resistance to EPO-induced differentiation to fetal hemoglobin (HbF)–positive erythroid cells, consistent with the role of oncogenic *IDH* mutations in promoting “stemness” by blocking cell differentiation (refs. 7, 9, 22, 23, 26; Fig. 1D and E).

Mutant IDH causes global epigenetic alterations by impairing histone and DNA demethylases (7–10). We observed increased histone methylation and 5-methylcytosine (5mC) and decreased 5-hydroxymethylcytosine (5hmC) in base-edited *IDH^{mut}* and *IDH^{mut}* TF-1 cells (Supplementary Fig. S1C and S1D). We also generated base-edited *IDH1^{WT/mut}* or *IDH2^{WT/mut}* K562 and MOLM-13 clonal leukemia cells and confirmed the significant increases of R-2HG (Supplementary Fig. S1B and S1E). These results demonstrate that the biological effects caused by base-edited *IDH^{mut}* are not dependent on specific cellular contexts or genetic background. Together, we created a panel of clinically relevant *IDH1* or *IDH2* monoallelic mutations in 24 independent clonal cell lines that faithfully recapitulate the naturally occurring heterozygous *IDH^{mut}* cancer cells, thus establishing the preclinical cell models for dissecting the biological consequences and determinants of therapy response to IDH inhibition.

Acquired Mutations Identified by Saturation Variant Screens

Having validated the base-edited *IDH1^{R132H}* and *IDH2^{R140Q}* leukemia cells, we designed orthogonal mutagenesis screens to identify *IDH* second-site mutations capable of conferring resistance to *IDH^{mut}* inhibitors. We reasoned that if *IDH^{mut}* cells acquire R-2HG–restoring mutations upon treatment with *IDH^{mut}* inhibitors (AG-120 or ivosidenib for *IDH1^{R132H}*, AG-221 or enasidenib for *IDH2^{R140Q}*), the cells would be resistant to EPO-induced differentiation and progressively enriched in undifferentiated HbF-negative cell populations. To this end, the *IDH2^{R140Q}-BE* cells were treated with 1 μ mol/L AG-221 continuously for 16 weeks, followed by EPO-induced differentiation for 8 days (2 U/mL) before FACS-sorting of HbF-negative cells. Targeted sequencing of the complete protein-coding sequences of the endogenous *IDH2* gene was performed in genomic DNA isolated in cells after short-term (6 weeks) or long-term (16 weeks) AG-221 treatment (Fig. 2A). From two replicate screens, we identified 109 enriched second-site mutations at 91 amino acid positions (fold change ≥ 2 in cells at 16 relative to 6 weeks) clustered at the small domains and the C-terminal large domain of *IDH2* (Fig. 2B; Supplementary Fig. S2A; Supplementary Table S3).

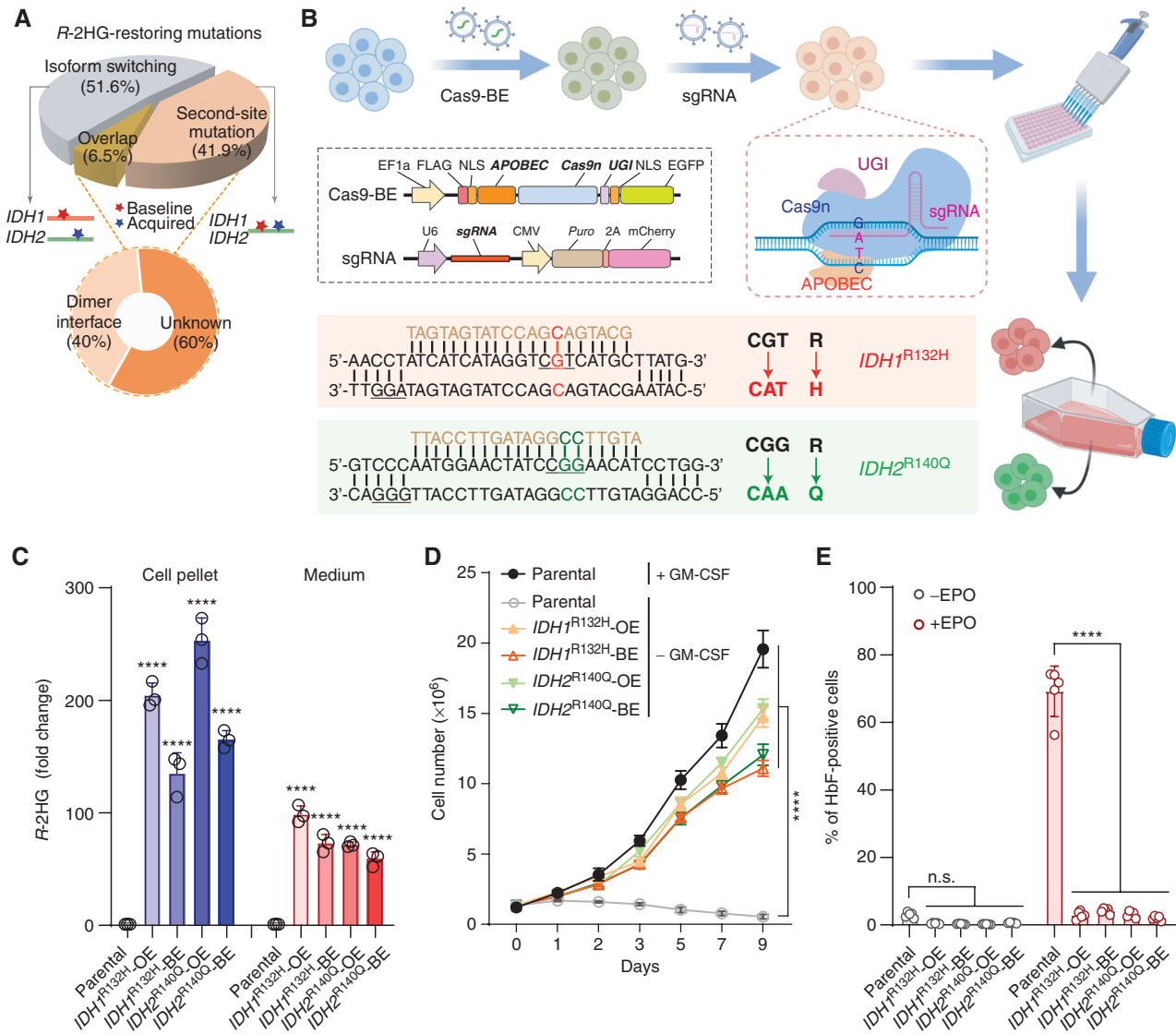


Figure 1. Generation of isogenic *IDH*^{mut} leukemia cells by CRISPR base editing. **A**, Distribution of acquired *R*-2HG–restoring mutations in relapsed or refractory AML patients after *IDH*^{mut} inhibitor treatment ($N = 31$ AML patients). **B**, Schematic of CRISPR base editing of *IDH1*^{R132H} or *IDH2*^{R140Q} in leukemia cells. Cells were transduced with Cas9-BE and sgRNAs targeting *IDH1* or *IDH2*. Single cell-derived clones containing the correct editing were validated by targeted sequencing. The edited nucleotides are shown as red and green for *IDH1*^{R132H} and *IDH2*^{R140Q}, respectively. The sgRNAs are shown in yellow, with protospacer adjacent motif (PAM) regions underlined. **C**, Increased *R*-2HG production in base-edited *IDH1*^{R132H} or *IDH2*^{R140Q} leukemia cells. Unmodified TF-1 cells and cells stably expressing *IDH1*^{R132H}-OE or *IDH2*^{R140Q}-OE (*IDH1*^{R132H}-OE or *IDH2*^{R140Q}-OE) were analyzed as controls. **D**, GM-CSF cytokine-independent growth of base-edited *IDH1*^{R132H} or *IDH2*^{R140Q} leukemia cells. **E**, The base-edited *IDH1*^{R132H} or *IDH2*^{R140Q} leukemia cells were resistant to EPO-induced erythroid differentiation. The percentage of differentiated cells (HbF-positive) with or without EPO induction for 8 days was determined by flow cytometry. Results are mean \pm SD ($N = 3$ or 5 independent experiments) and analyzed by a one-way or two-way ANOVA. ****, $P < 0.0001$. n.s., not significant.

The AG-221 selection screen uncovered candidate second-site mutations associated with acquired resistance but did not provide a complete assessment of all possible variants due to low frequency of spontaneous mutations. We next designed the second screen using a saturation variant library consisting of full-length *IDH2* cDNAs harboring amino acid substitutions. We validated the presence of 7,742 individual *IDH2*-mutant cDNAs in which each amino acid at positions 41 to 452 (excluding mitochondrial localization signal and stop codon) was replaced by one of the other 19 amino acids (Fig. 2C; Supplementary Table S4). The saturation variant library was then cloned into a lentiviral vector and

transduced into *IDH2*^{R140Q}-BE cells at a multiplicity of infection (MOI) ≤ 0.3 , such that the vast majority of cells received only one mutant cDNA. The transduced cells were selected, treated with 1 $\mu\text{mol/L}$ AG-221 (0 to 10 weeks), and induced by EPO for 8 days before harvesting genomic DNA from HbF-negative cells. By targeted sequencing of *IDH2*-mutant cDNA in cells after AG-221 treatment (0, 2, 4, 6, 8, and 10 weeks or T0 to T5, respectively; Fig. 2C), we identified 245 progressively enriched second-site mutations at 187 amino acid positions (fold change ≥ 2 in T5 relative to T0) from two replicate screens (Fig. 2D; Supplementary Fig. S2B; Supplementary Table S5).

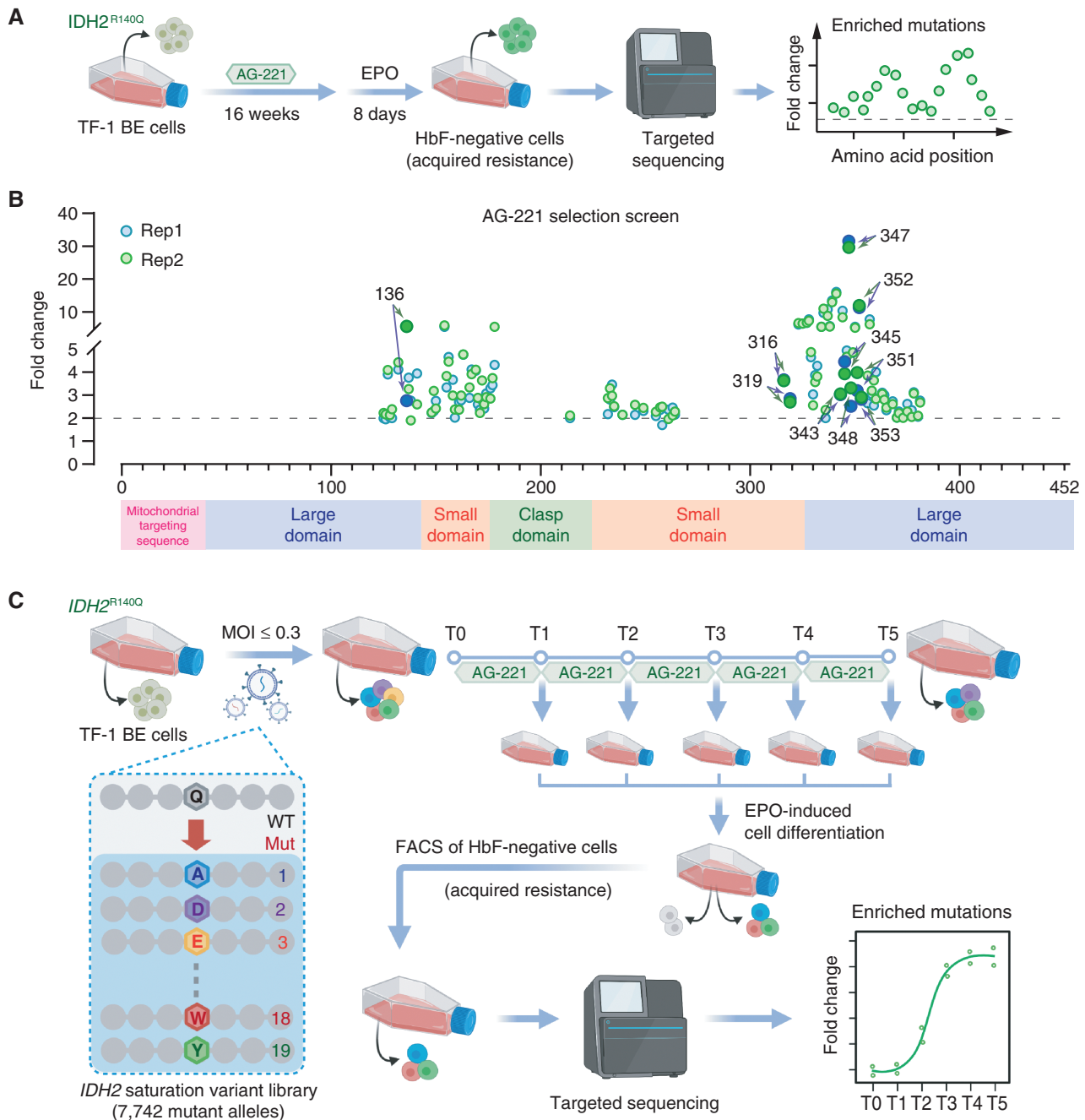


Figure 2. Identification of *IDH2* second-site mutations by mutagenesis screens. **A**, Schematic of AG-221 selection screens to identify *IDH2* second-site mutations associated with acquired resistance in *IDH2*^{R140Q}-BE cells. Targeted sequencing of *IDH2* exons was performed using genomic DNA isolated in HbF-negative cells after short-term (6 weeks) and long-term (16 weeks) AG-221 treatment. **B**, *IDH2* second-site mutations identified from AG-221 selection screens. The enriched mutations (fold change ≥ 2 ; y-axis) from two independent screens (rep1 and rep2) are shown with the amino acid positions (1–452; x-axis). The annotated protein domains are shown on the bottom. **C**, Schematic of saturation variant screens to identify *IDH2* second-site mutations associated with acquired resistance in *IDH2*^{R140Q}-BE cells. *IDH2*^{R140Q}-BE cells were transduced with variant library at MOI ≤ 0.3 , selected with AG-221 for various durations, and induced by EPO before targeted sequencing of *IDH2* exons in HbF-negative cells after AG-221 treatment (0, 2, 4, 6, 8, and 10 weeks or T0 to T5, respectively). Mut, mutant; WT, wild-type. (continued on following page)

Together, second-site mutations at 43 amino acid positions in *IDH2* were consistently identified in AG-221 selection and saturation variant screens. The identification of known mutations at the dimer interface (*IDH2*^{Q316E} and *IDH2*^{I319M}) provides support for the performance of both screens (ref. 15;

Fig. 2D and E). More importantly, by mapping these positions on the structure of inhibitor-bound *IDH2*^{R140Q} homodimer (12), we uncovered a previously unrecognized class of mutations at residues N136, E343, E345, A347, H348, V351, T352, and R353, which physically surround and interact

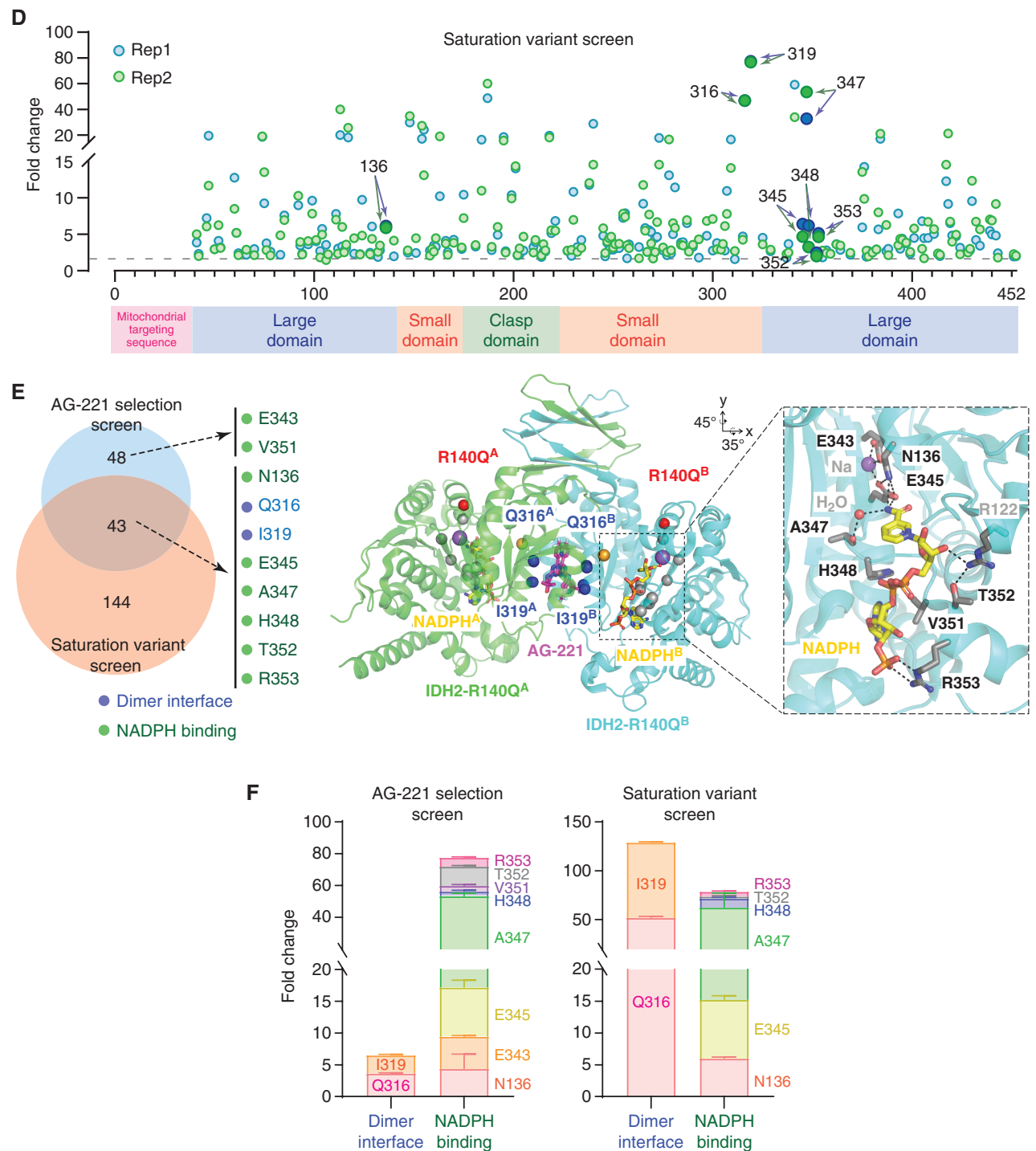


Figure 2. (Continued) D, IDH2 second-site mutations identified from saturation variant screens. The progressively enriched mutations (fold change ≥ 2 ; y-axis) from two independent screens (rep1 and rep2) are shown with the amino acid positions (1–452; x-axis). **E**, Identification of IDH2 second-site mutations from orthogonal screens. Mutations at the dimer interface and NADPH binding sites are shown on the left as blue and green, respectively. The structure of inhibitor-bound IDH2^{R140Q} homodimer in the open conformation (PDB #5196) is shown on the right. Gray spheres represent the C-alpha atoms of the identified residues at the NADPH binding sites on chains A and B of the IDH2^{R140Q} homodimer, respectively. Sodium and calcium ions are shown as purple and orange spheres, respectively. Binding of AG-221 (pink) at the dimer interface and C-alpha atoms of IDH2^{R140Q} (red spheres) are shown. The close-up view of the active site containing NADPH (yellow) is also shown. The residues associated with second-site mutations are indicated on the structure. **F**, The enrichment of second-site mutations at the dimer interface or NADPH binding sites of IDH2^{R140Q} is shown for AG-221 selection screens (left) and saturation variant screens (right). (continued on next page)

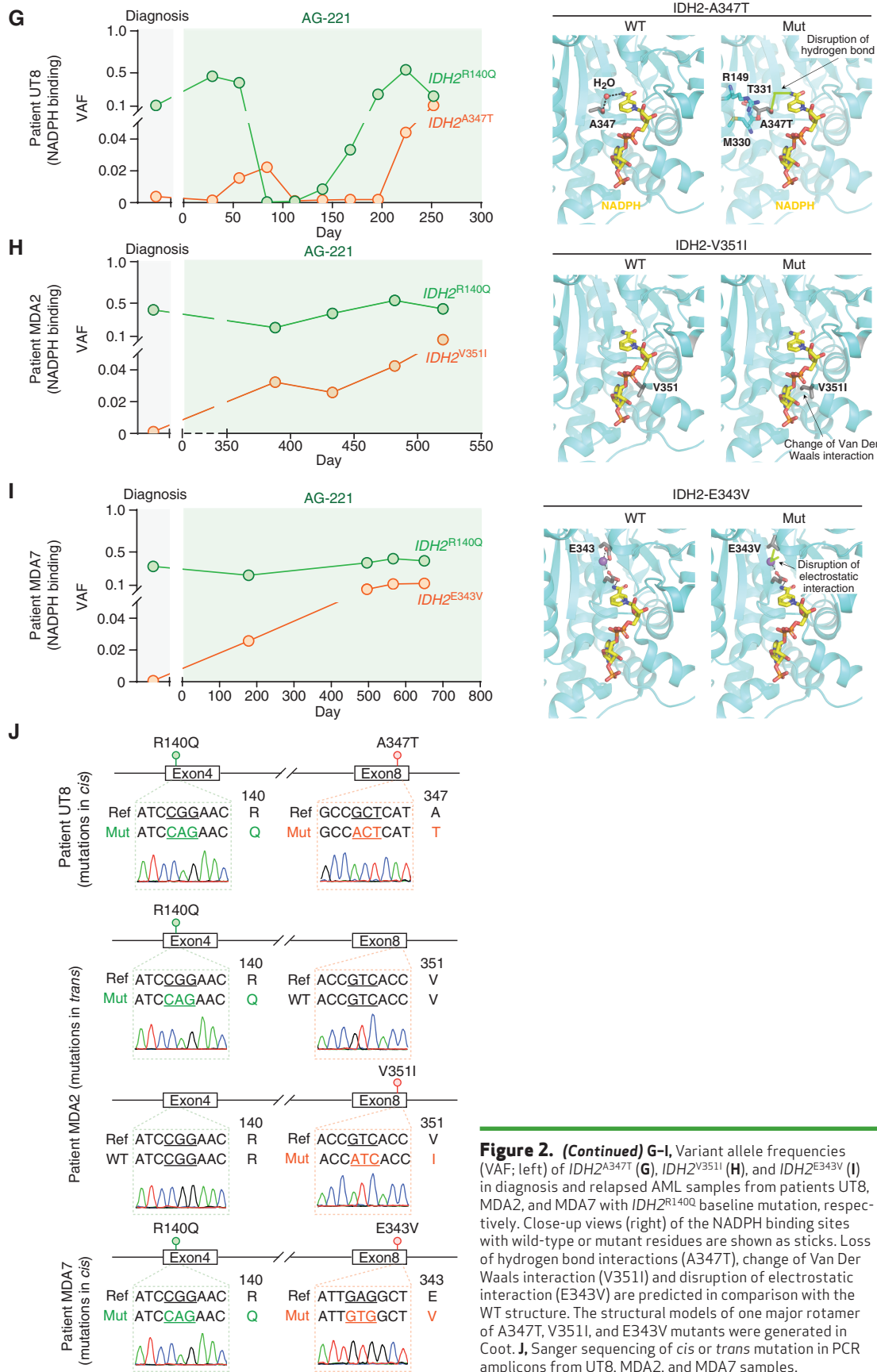


Figure 2. (Continued) G-I, Variant allele frequencies (VAF; left) of IDH2^{A347T} (G), IDH2^{V351I} (H), and IDH2^{E343V} (I) in diagnosis and relapsed AML samples from patients UT8, MDA2, and MDA7 with IDH2^{R140Q} baseline mutation, respectively. Close-up views (right) of the NADPH binding sites with wild-type or mutant residues are shown as sticks. Loss of hydrogen bond interactions (A347T), change of Van Der Waals interaction (V351I) and disruption of electrostatic interaction (E343V) are predicted in comparison with the WT structure. The structural models of one major rotamer of A347T, V351I, and E343V mutants were generated in Coot. J, Sanger sequencing of *cis* or *trans* mutation in PCR amplicons from UT8, MDA2, and MDA7 samples.

with NADPH cofactor at the enzyme active site via a series of hydrogen bonding, hydrophobic, electrostatic, and/or Van Der Waals interactions (Fig. 2E). For example, the carboxyl group of residue E343 forms sodium ion and E345-mediated indirect interactions with the amino group of the reduced nicotinamide moiety of NADPH, whereas the main chain atoms of residue A347 contact the same chemical group of NADPH through solvent-mediated hydrogen bonds (Fig. 2E). Moreover, the enrichment of mutations at the NADPH binding sites was comparable with or higher than the enrichment of mutations at the dimer interface (Fig. 2F).

Second-Site Mutations Affecting NADPH Binding Identified in AML Patients

To assess the clinical relevance, we analyzed a cohort of 24 relapsed or refractory AML cases with *IDH1* or *IDH2* baseline mutations who developed resistance after treatment with IDH inhibitors (Supplementary Fig. S2C; Supplementary Table S6). By targeted sequencing of the complete protein-coding sequences of *IDH1* and *IDH2* genes in matched pre- and posttreatment bone marrow specimens, we identified seven cases with *IDH1*^{R132C}, *IDH1*^{R132H}, or *IDH2*^{R140Q} baseline mutations at diagnosis that acquired *R-2HG*-restoring mutations in relapse samples. These include one case of a dimer interface mutation (*IDH2*^{I319M} in patient UT6) and two cases of isoform-switching mutations (*IDH1*^{R132C} to *IDH2*^{R140Q} in UT5 and *IDH1*^{R132H} to *IDH2*^{R140Q} in UT9; Supplementary Fig. S2D–S2F), consistent with the role of these mutations in driving acquired resistance to IDH inhibition (15, 16).

Importantly, we identified three cases of *IDH2* second-site mutations at the NADPH binding sites, including A347T in UT8, V351I in MDA2, and E343V in MDA7 (Fig. 2G–I; Supplementary Fig. S2G), which were among the top candidates identified in AG-221 selection or saturation variant screens (Fig. 2A–F). Structural analysis indicates that the side chain packing of residue A347 is changed by this mutation such that residues A347 and H348 move away from their locations in the wild-type conformation to attenuate NADPH association (Fig. 2G). Importantly, the other mutations (N136S, E343V, E345G, H348Q, V351I, T352A, and R353H) were also predicted to impact NADPH binding by disrupting hydrogen bond, electrostatic, and/or Van Der Waals interactions (Fig. 2H and I; Supplementary Fig. S2H). Moreover, we analyzed longitudinal samples of UT8, MDA2, and MDA7 harboring NADPH binding site mutations. We observed progressive increases in variant allele frequencies (VAF) across posttreatment samples, indicating a positive selection of second-site mutations in response to IDH inhibition (Fig. 2G–I). Besides these mutations, N136S was previously described in an AML case with *IDH2*^{R172K} baseline mutation (27).

We next performed PCR and Sanger sequencing using genomic DNA and confirmed the *cis* configuration for *IDH2*^{WT} + *IDH2*^{R140Q+A347T} in UT8 and *IDH2*^{WT} + *IDH2*^{R140Q+E343V} in MDA7 but the *trans* configuration for *IDH2*^{R140Q} + *IDH2*^{V351I} in MDA2, respectively (Fig. 2J). To determine whether the same mutation can occur in *cis* or *trans*, we analyzed the mutation patterns in cDNAs of base-edited leukemia cells from the AG-221 selection screens by amplicon sequencing (Supplementary Fig. S2I; Supplementary Table S7). We found that A347T, V351I, and E343V

were detected in both *cis* and *trans* configurations in different sequencing reads (Supplementary Fig. S2J).

To corroborate these findings, we performed similar screens in *IDH1*^{R132H}-BE cells after treatment with 1 μmol/L AG-120 for 16 weeks (Supplementary Fig. S3A). We identified *IDH1*^{S280F}, a mutation known to affect allosteric binding of AG-120 at the dimer interface (15, 17), as one of the top candidates (Supplementary Fig. S3B and S3C; Supplementary Table S8). More importantly, by comparing the acquired mutations from AG-120 inhibitor screens with *R-2HG*-restoring mutations identified in *IDH1*-mutant AML patients treated with AG-120 (Supplementary Tables S1 and S6; ref. 17), we not only confirmed the recurrent dimer interface mutation at *IDH1*^{S280F} (15, 17) but also uncovered two NADPH binding-associated mutations at *IDH1*^{T313I} and *IDH1*^{H315D}, respectively (Supplementary Fig. S3D). *IDH1*^{T313I} displayed progressive increases of VAFs in patient MDA4 following AG-120 treatment (Supplementary Fig. S3E), whereas *IDH1*^{H315D} was detected in a relapsed AML case with VAF around 30% and associated with restored *R-2HG* in the relapsed samples following AG-120 monotherapy (17). These mutations are predicted to weaken NADPH binding by disturbing hydrogen bond interactions based on the structure of inhibitor-bound *IDH1*^{R132H} (PDB #5L57; ref. 28; Supplementary Fig. S3F) and were detected in both *cis* and *trans* configurations in AG-120-treated TF-1 cells (Supplementary Fig. S3G). Therefore, our orthogonal screens in base-edited *IDH*^{mut} leukemia cells revealed a compendium of clinically relevant second-site mutations, enabling a detailed dissection of the underlying mechanisms for acquired resistance to IDH inhibition.

R-2HG-Restoring Mutations Mediate Acquired Resistance to IDH Inhibition

The identification of recurrent second-site mutations affecting NADPH cofactor binding raises the question about their effects on *R-2HG* production and the catalytic function of *IDH*^{mut} proteins. To address this, we generated TF-1 cells stably expressing *IDH2*^{R140Q} with or without each second-site mutation and measured *R-2HG* levels after treatment with control (DMSO) or 1 μmol/L AG-221 for 3 days. AG-221 treatment significantly decreased *R-2HG* in *IDH2*^{R140Q}-expressing cells without second-site mutation, consistent with the effective inhibition of *IDH2*^{mut}-catalyzed *R-2HG* production (4–6). By contrast, expression of *IDH2*^{R140Q} harboring second-site mutation associated with NADPH binding blocked AG-221-mediated inhibition, resulting in restored *R-2HG* similar to that observed in DMSO-treated cells or cells with the dimer interface mutations (Fig. 3A). Similarly, the *IDH1*^{T313I} and *IDH1*^{H315D} mutations associated with NADPH binding also blocked AG-120-mediated inhibition in *IDH1*^{R132H}-expressing TF-1 cells, causing *R-2HG* accumulation to the level observed with *IDH1*^{S280F} at the dimer interface (Fig. 3B).

As mutant IDH catalyzes the reduction of αKG to *R-2HG* by oxidizing NADPH (4, 5), we determined the effect of second-site mutations on IDH catalytic activity by measuring NADPH consumption in *IDH2*^{R140Q}-expressing TF-1 cells (Fig. 3C). Of note, AG-221 effectively inhibited the catalytic activity of *IDH2*^{R140Q}, resulting in significantly decreased NADPH consumption in *IDH2*^{R140Q}-expressing cells. By contrast, the presence of second-site mutations at NADPH

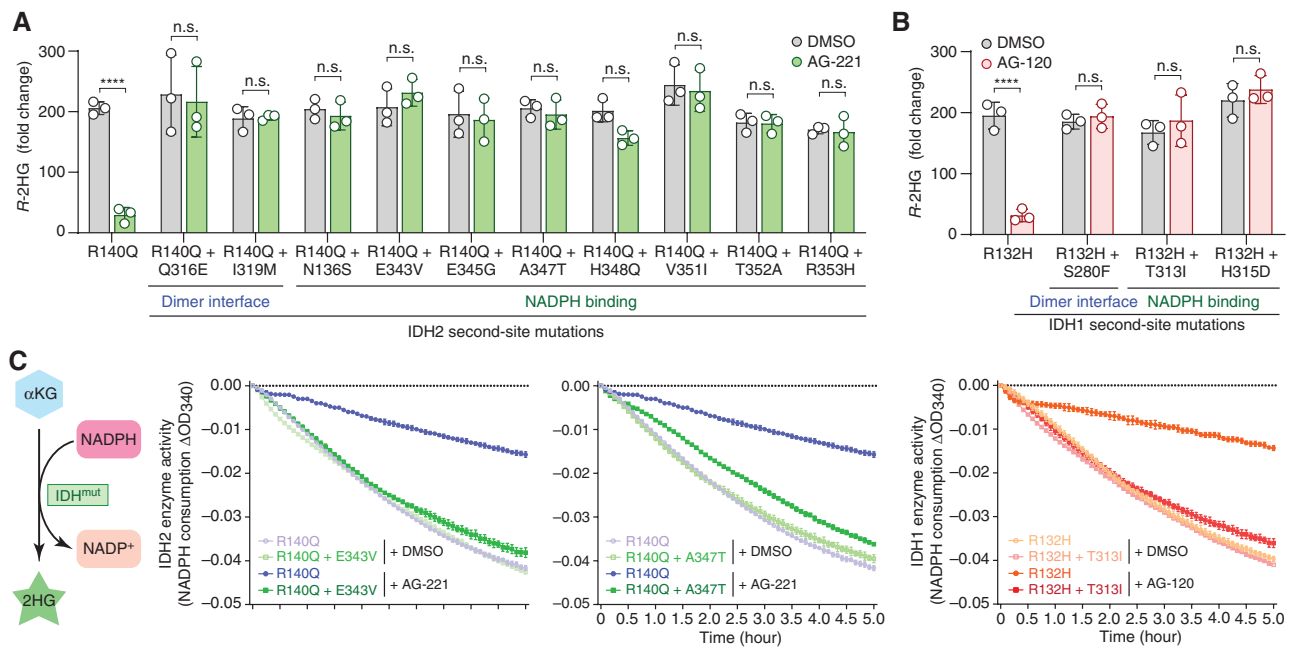


Figure 3. R-2HG-restoring mutations mediate resistance to IDH inhibition. **A**, IDH2 second-site mutations acting in *cis* at the dimer interface or NADPH binding sites restored R-2HG levels in TF-1 cells treated with AG-221. Cells stably expressing IDH2^{R140Q} alone were analyzed as controls. Results are mean \pm SD ($N = 3$ independent experiments). **B**, IDH1 second-site mutations at the dimer interface or NADPH binding sites restored R-2HG in TF-1 cells treated with AG-120. Results are mean \pm SD ($N = 3$ independent experiments). **C**, IDH second-site mutations restored the catalytic activity of IDH^{mut} enzymes upon inhibitor treatment. NADPH consumption was measured using cell lysates from TF-1 cells expressing IDH2^{R140Q} alone or with E343V (left) or A347T (right) treated with DMSO or AG-221, or TF-1 cells expressing IDH1^{R132H} alone or with T313I (bottom) treated with DMSO or AG-120. Results are mean \pm SD ($N = 3$ independent measurements). (continued on following page)

binding sites resulted in similar rates of NADPH consumption as observed with dimer interface mutations (IDH2^{Q316E} and IDH2^{I319M}) or DMSO-treated cells (Fig. 3C; Supplementary Fig. S4A–S4H). Similar results were obtained for IDH1^{T313I}, IDH1^{S280F}, or IDH1^{H315D} in IDH1^{R132H}-expressing TF-1 cells (Fig. 3C; Supplementary Fig. S4K and S4L). The mutation of residues not associated with NADPH binding did not affect IDH^{mut} activity or R-2HG production in the presence of inhibitors (Supplementary Figs. S4I–S4N and S5A and S5B). Moreover, these second-site mutations alone did not induce R-2HG production and had no effect on cytokine-dependent cell growth or EPO-induced HbF expression (Supplementary Fig. S5C–S5F).

To further evaluate whether the identified mutations promote therapy resistance *in vivo*, we xenografted IDH2^{R140Q}-expressing TF-1 cells with or without second-site mutations into the NSG-SGM3 (or NSGS) transgenic mice expressing human IL3, GM-CSF, and SCF that support the stable engraftment of human myeloid leukemia cells (29). These mice were engrafted with mCherry and luciferase-marked TF-1 cells expressing IDH2^{R140Q} alone or with second-site mutation (IDH2^{E343V} or IDH2^{A347T}). After disease onset, the mice were treated with vehicle or 30 mg/kg AG-221 and monitored for leukemia development (Fig. 3D). AG-221 treatment impaired the propagation of leukemia cells, resulting in less tumor burden, fewer leukemic cells in peripheral blood and bone marrow, and prolonged survival compared with vehicle-treated controls. By contrast, the presence of a second-site mutation rendered IDH2^{R140Q}-expressing cells resistant to

AG-221 inhibition, resulting in leukemia burden comparable with vehicle-treated controls (Fig. 3E–H). The presence of NADPH binding-associated IDH1^{T313I} or IDH1^{H315D} in IDH1^{R132H}-expressing TF-1 cells also induced resistance to AG-120 treatment in xenografted mice (Supplementary Fig. S6A–S6E). Collectively, these results establish a functional role for NADPH binding site-associated mutations in restoring R-2HG production to drive resistance to IDH inhibition.

NADPH-Dependent Uncompetitive Inhibition of Mutant IDH Heterodimers

Having validated the *in vivo* efficacy of NADPH binding-associated mutations in conferring therapy resistance, we determined the extent to which the second-site mutation affects inhibitor function. To this end, we first determined R-2HG production in TF-1 cells expressing IDH2^{R140Q} with or without A347T second-site mutation in the presence of AG-221 (10^{-5} to 100 $\mu\text{mol/L}$). AG-221 impaired R-2HG production in cells with IDH2^{R140Q} alone starting at 1 nmol/L with maximal inhibition at ≥ 1 $\mu\text{mol/L}$ concentration. By contrast, cells coexpressing IDH2^{R140Q} and A347T increased the threshold of AG-221 inhibition to 50 $\mu\text{mol/L}$ or higher concentration (Fig. 4A). We next measured the enzyme activity of IDH2^{R140Q} with or without A347T in the presence of AG-221 (10^{-5} to 100 $\mu\text{mol/L}$) in TF-1 cells. AG-221 effectively blocked IDH2^{R140Q} activity at 0.1 to 1 nmol/L with maximal inhibition at 0.1 to 1 $\mu\text{mol/L}$ concentration (Fig. 4B). By contrast, IDH2^{R140Q} with A347T significantly increased the threshold of AG-221 inhibition. These studies indicate that

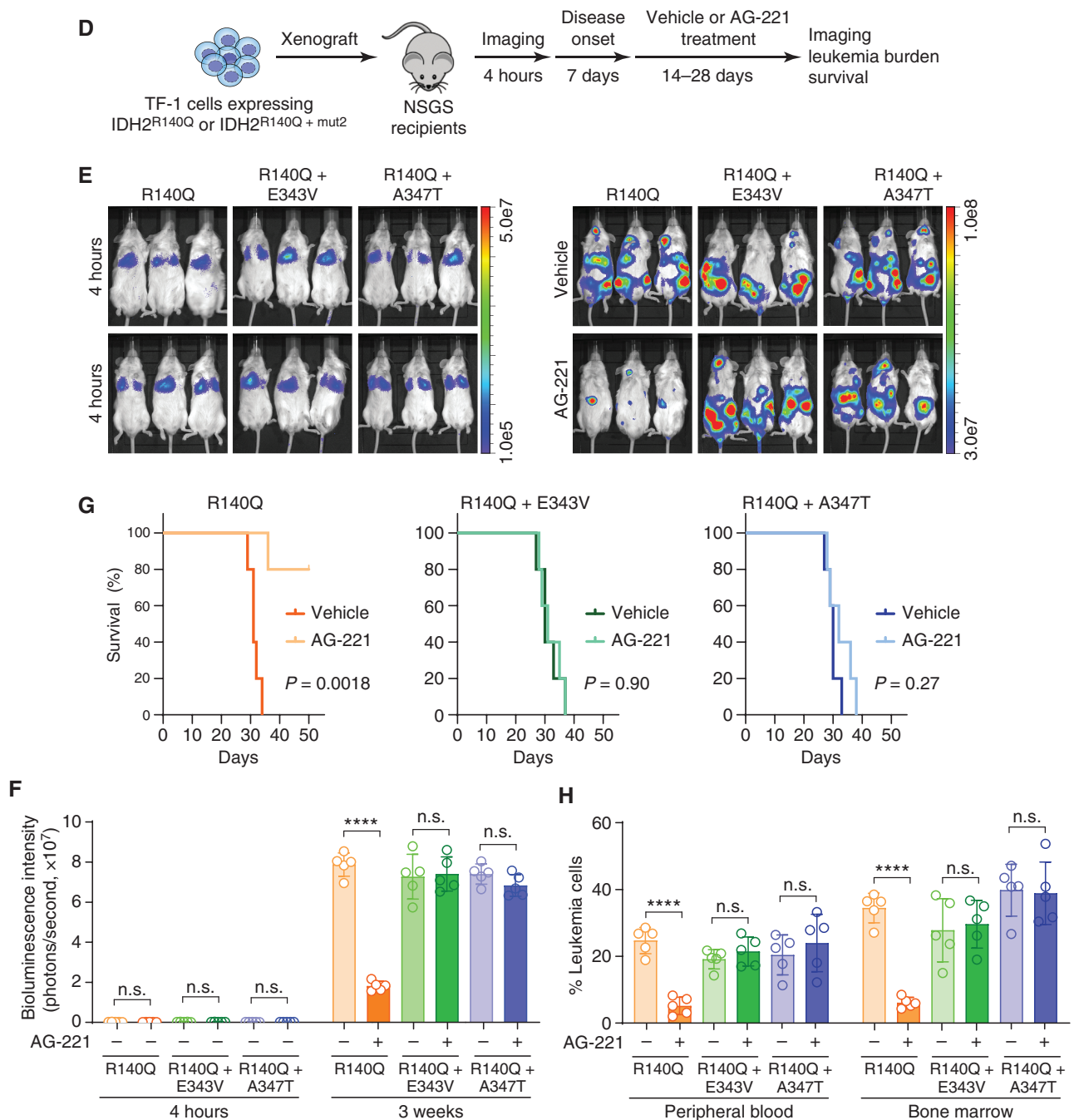


Figure 3. (Continued) **D**, Schematic of *in vivo* xenotransplantation assays. **E**, IDH2 second-site mutations at NADPH binding sites (E343V and A347T) conferred resistance to AG-221 in mice. Bioluminescence intensity is shown for NSGS mice xenografted with TF-1 cells stably expressing IDH2^{R140Q} alone or with second-site mutations at 4 hours and 28 days (or moribund mice) with vehicle or AG-221 treatment. **F**, Quantification of bioluminescence intensity for xenografted NSGS mice. Results are mean \pm SD ($N = 5$ mice per group). **G**, Kaplan-Meier survival curves of NSGS mice xenografted with TF-1 cells stably expressing IDH2^{R140Q} alone (left) or with E343V (middle) or A347T (right) treated with vehicle or AG-221 ($N = 5$ mice per group). P values by a log-rank Mantel-Cox test. **H**, Quantification of leukemia burden in peripheral blood and bone marrow of xenografted NSGS mice at 28 days (or moribund mice) after transplantation. Results are mean \pm SD ($N = 5$ mice per group) and analyzed by a two-way ANOVA. ****, $P < 0.0001$. n.s., not significant.

the NADPH binding site mutations increase the threshold of inhibitor binding, thus requiring higher inhibitor concentrations to block IDH^{mut}-catalyzed *R*-2HG production. Moreover, the NADPH binding site mutations also restored IDH^{mut}-mediated *R*-2HG production in TF-1 cells treated with other IDH^{mut} inhibitors including AG-881 (vorasidenib,

ref. 30; IDH-305, ref. 31; or BAY-1436032, ref. 32; Fig. 4C and D; Supplementary Fig. S6F and S6G).

Wild-type IDH enzymes convert ICT to α KG and generate NADPH, whereas oncogenic IDH^{mut} proteins gain the activity of reducing α KG to *R*-2HG and convert NADPH to NADP⁺. Consistent with the neomorphic activity of IDH^{mut} enzymes,

IDH1^{R132H}- and IDH2^{R140Q}-expressing cells significantly decreased intracellular NADPH and increased NADP⁺ in TF-1 cells (Fig. 4E). IDH1^{mut} and IDH2^{mut} inhibitors restored NADPH levels in IDH1^{R132H}- and IDH2^{R140Q}-expressing cells, respectively, indicating effective blocking of IDH^{mut} enzyme activity (Fig. 4F). However, NADPH levels remained low in inhibitor-treated TF-1 cells coexpressing IDH1^{R132H} with IDH1^{H315D} (or IDH2^{R140Q} with IDH2^{A347T}) second-site mutation (Fig. 4F). These findings demonstrate that secondary mutations at NADPH binding sites restore the neomorphic activity of IDH^{mut} enzymes in the presence of IDH inhibitors.

Both AG-120 and AG-221 show slow-tight binding inhibition to IDH1^{R132H} and IDH2^{R140Q}, respectively (12, 33). The binding of IDH inhibitors to the dimer interface of IDH^{mut} homodimers stabilizes the inactive open conformation and prevents conformational change to block IDH^{mut}-catalyzed R-2HG production (12, 22, 34). Moreover, AG-221 is an uncompetitive inhibitor (Fig. 5A) with regard to NADPH and NADP⁺ based on the studies using IDH2^{mut} and IDH2^{WT} homodimers, respectively (12). Cancer-associated *IDH* mutations occur in a single allele, resulting in the formation of a mixture of IDH^{WT/mut} heterodimers and IDH^{mut} homodimers. As the IDH^{WT/mut} heterodimers produce R-2HG more efficiently than IDH^{mut} homodimers (35), they are considered the major molecular targets for therapeutic inhibition. Despite these findings, previous biochemical and structural studies were based on IDH^{mut} homodimers (12, 22, 33, 34), whereas the mode of inhibition for IDH^{WT/mut} heterodimers has not been evaluated.

To this end, we tested whether IDH inhibitors exhibit uncompetitive inhibition with regard to NADPH using purified IDH1^{WT/R132H} and IDH2^{WT/R140Q} heterodimers. By titration series of substrates versus fixed concentrations of inhibitors, we observed that the linear regression fits of the reciprocal plots yielded parallel lines for both IDH1^{WT/R132H}-AG-120 and IDH2^{WT/R140Q}-AG-221 complexes (Fig. 5B and C), consistent with an uncompetitive model of inhibition (36). Therefore, both AG-120 and AG-221 act as uncompetitive inhibitors with regard to NADPH on the clinically relevant IDH^{WT/mut} heterodimers. A prerequisite for the mode of uncompetitive inhibition is that the IDH^{mut}-NADPH complex must be formed to allow the binding of the IDH^{mut} inhibitor and that inhibitor binding facilitates the formation of the stable IDH^{mut}-inhibitor complex (Fig. 5A).

Acquired Resistance by Disabling Uncompetitive Enzyme Inhibition

Based on the biochemical studies, we hypothesized that the binding of NADPH is critical for the formation of stable IDH^{mut}-inhibitor complexes and that secondary mutations

at NADPH binding sites promote acquired resistance by disabling uncompetitive enzyme inhibition. Given the more potent activity of IDH^{WT/mut} heterodimers in catalyzing R-2HG production (35), we focused on IDH1^{WT/R132H} and IDH2^{WT/R140Q} for subsequent studies.

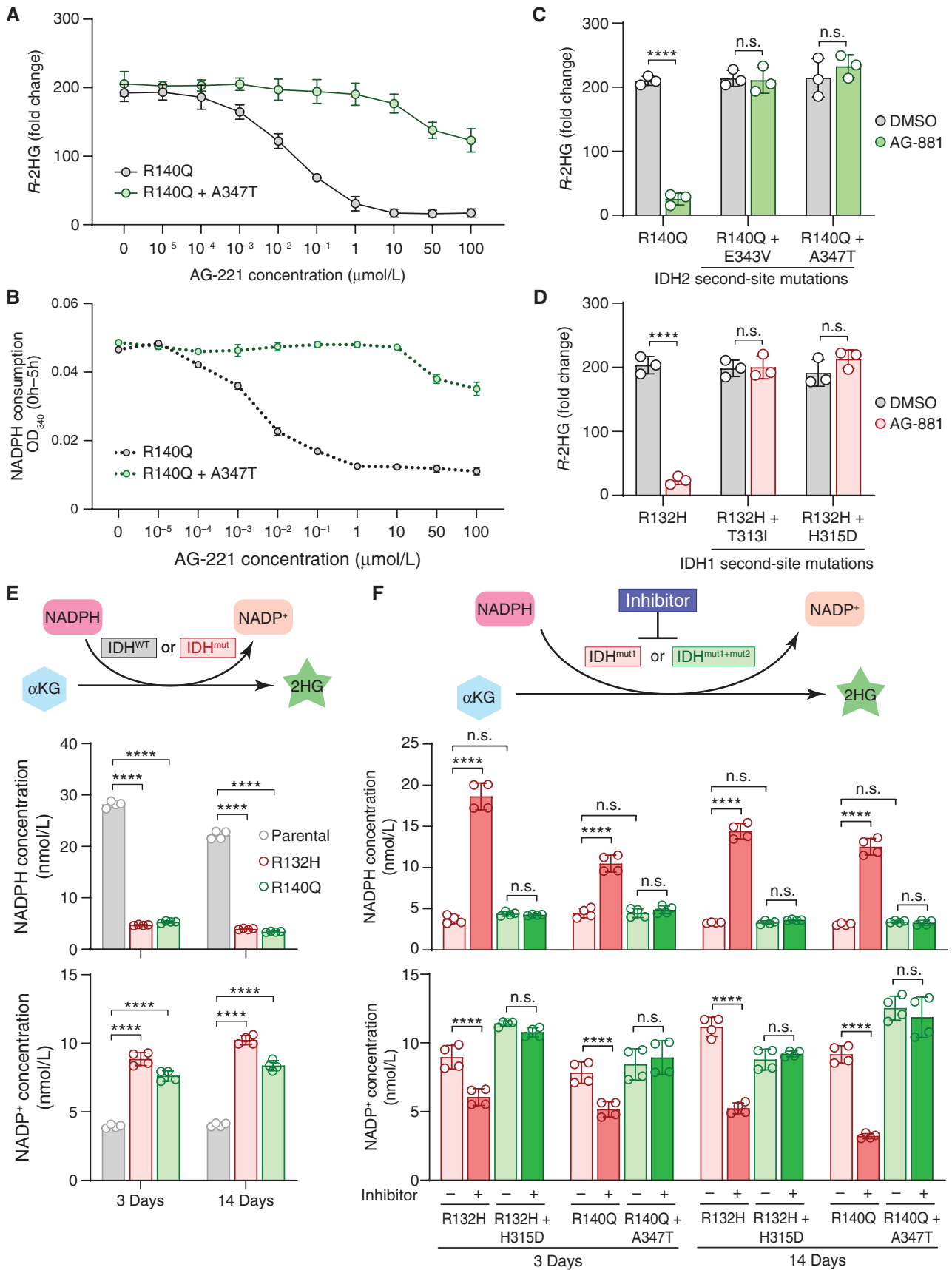
We isolated IDH^{WT/mut} heterodimers without (IDH^{WT} + IDH^{mut1}) or with (IDH^{WT} + IDH^{mut1+mut2}) second-site mutations by coexpressing GST-tagged IDH^{WT} and 6xHis-tagged IDH^{mut}, followed by tandem affinity purification in *Escherichia coli* Rosetta2 (DE3) cells (Fig. 5D). Specifically, we purified heterodimers containing IDH2^{R140Q} alone or with secondary mutations at the dimer interface (IDH2^{R140Q+Q316E} and IDH2^{R140Q+H319M}) or NADPH binding sites (IDH2^{R140Q+E343V} and IDH2^{R140Q+A347T}; Fig. 5E). Of note, the binding affinity (K_m) of NADPH to IDH2^{R140Q+Q316E} and IDH2^{R140Q+H319M} was comparable with IDH2^{R140Q} alone (Fig. 5F and G), consistent with the role of these mutations in preventing allosteric inhibitor binding to dimer interface without affecting NADPH binding at the active site. By contrast, NADPH binding affinity to IDH2^{R140Q+E343V} and IDH2^{R140Q+A347T} was lower than IDH2^{R140Q} alone ($K_m = 5.66 \pm 0.27 \mu\text{mol/L}$ and $4.64 \pm 0.77 \mu\text{mol/L}$ for IDH2^{R140Q+E343V} and IDH2^{R140Q+A347T} vs. $K_m = 3.51 \pm 0.19 \mu\text{mol/L}$ for IDH2^{R140Q}; Fig. 5F and G). Moreover, the half maximal inhibitory concentration (IC₅₀) was higher for heterodimers containing dimer interface or NADPH binding site mutations than IDH2^{R140Q} alone (Fig. 5F and H), illustrating impaired inhibitor binding by both types of mutations. Lastly, although IDH^{mut} enzyme activity was impaired by AG-221-mediated inhibition of IDH2^{R140Q}, second-site mutations at the dimer interface or NADPH binding sites restored IDH2^{R140Q} activity in the presence of AG-221 (Fig. 5I). It is important to note that the modest changes in NADPH and inhibitor binding *in vitro* were associated with significant increases in R-2HG production in TF-1 cells, likely due to the differences in substrate and enzyme concentrations used for *in vitro* biochemical assays.

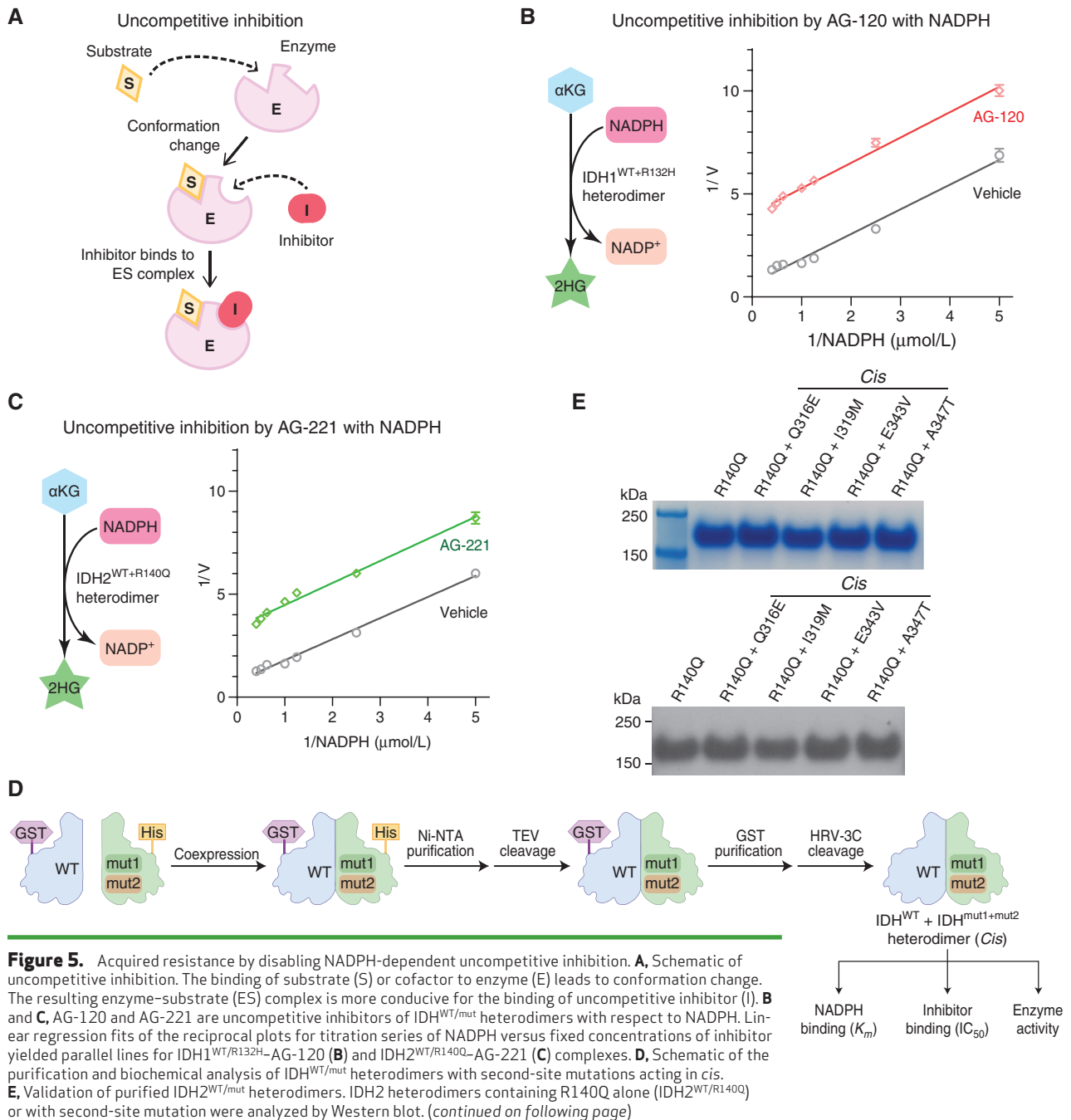
To corroborate these findings, we examined the effects of NADPH binding site-associated IDH1^{T313I} or IDH1^{H315D} mutation in IDH1^{R132H} heterodimers. IDH1^{T313I} or IDH1^{H315D} also decreased NADPH and inhibitor binding, resulting in restored IDH1^{R132H} activity upon AG-120 treatment (Supplementary Fig. S7A–S7E). Therefore, secondary mutations at NADPH binding sites decreased NADPH binding to prevent the formation of stable IDH^{mut}-inhibitor complexes, resulting in restored IDH^{mut} activity in the presence of inhibitors.

Disabling Uncompetitive Inhibition by Acting in Cis or Trans

Acquired resistance caused by dimer interface mutations can occur in *cis* on the IDH^{mut} allele or in *trans* on the opposite IDH^{WT} allele in human patients (15). The NADPH binding

Figure 4. Mutant IDH activity affects intracellular NADPH and NADP⁺ levels. **A**, R-2HG production in TF-1 cells expressing IDH2^{R140Q} alone or with A347T in *cis* treated with varying doses of AG-221. Results are mean \pm SD ($N = 3$ independent experiments). **B**, The relative catalytic activity of IDH2^{R140Q} alone or with A347T mutation in *cis* treated with varying doses of AG-221. NADPH consumption was measured using lysates from TF-1 cells expressing IDH2^{R140Q} with or without A347T treated with AG-221. Results are mean \pm SD ($N = 3$ independent experiments). **C** and **D**, IDH2 second-site mutations (E343V and A347T; **C**) and IDH1 second-site mutations (T313I and H315D; **D**) acting in *cis* at the NADPH binding sites restored R-2HG levels in TF-1 cells treated with the IDH dual inhibitor AG-881. Cells stably expressing IDH2^{R140Q} or IDH1^{R132H} alone were analyzed as controls. Results are mean \pm SD ($N = 3$ independent experiments). **E**, IDH1^{R132H}- or IDH2^{R140Q}-catalyzed R-2HG production decreased NADPH and increased NADP⁺ in leukemia cells. NADPH and NADP⁺ concentrations were determined in parental TF-1 cells (control) and cells stably expressing IDH1^{R132H} or IDH2^{R140Q} after 3 or 14 days of culture. Results are mean \pm SD ($N = 4$ independent experiments). **F**, Second-site mutations acting in *cis* at H315D or A347T restored IDH1^{R132H}- or IDH2^{R140Q}-catalyzed R-2HG production, decreased NADPH, and increased NADP⁺ in inhibitor-treated leukemia cells. NADPH and NADP⁺ concentrations were determined in TF-1 cells stably expressing IDH1^{R132H} (or IDH2^{R140Q}) alone or with second-site mutations after 3 or 14 days of culture with or without inhibitor, respectively. Results are mean \pm SD ($N = 4$ independent experiments) and analyzed by a two-way ANOVA. ****, $P < 0.0001$. n.s., not significant.





site mutations were also detected in *cis* or *trans* configuration in AML patients and cells. As our functional and biochemical studies of IDH second-site mutations focused on the *cis* configuration, it remains unknown whether and how disabling uncompetitive inhibition confers acquired resistance by acting in *trans*. IDH^{WT/mut} heterodimer consists of an IDH^{WT} monomer capable of catalyzing NADP⁺-dependent ICT to α KG conversion and an IDH^{mut} monomer catalyzing NADPH-dependent α KG to R-2HG conversion (4). We noted that the IDH^{mut} inhibitors AG-120 and AG-221 also exhibited uncompetitive inhibition with regard to NADP⁺ on purified IDH1^{WT/R132H} and IDH2^{WT/R140Q} heterodimers, respectively (Fig. 6A and B), consistent with previous findings

using IDH1^{WT} and IDH2^{WT} homodimers (12, 33). Based on these results, we reasoned that second-site mutations may act in *trans* by disabling NADP⁺-dependent uncompetitive inhibition of IDH^{WT} monomer to impair inhibitor binding and restore the catalytic function of IDH^{WT/mut} heterodimers.

To test this, we purified IDH2 heterodimers containing IDH2^{R140Q} alone or with second-site mutations in *trans* (IDH2^{R140Q} + IDH2^{E343V} or IDH2^{R140Q} + IDH2^{A347T}; Fig. 6C and D). We first noted decreased NADP⁺ binding affinity to IDH2^{E343V} and IDH2^{A347T} but not IDH2^{Q316E} and IDH2^{I319M} homodimers, consistent with impaired NADP⁺ binding due to E343V and A347T mutations (Fig. 6E and F). Moreover, we observed lower inhibitor binding affinity to IDH2^{R140Q} + IDH2^{E343V} and

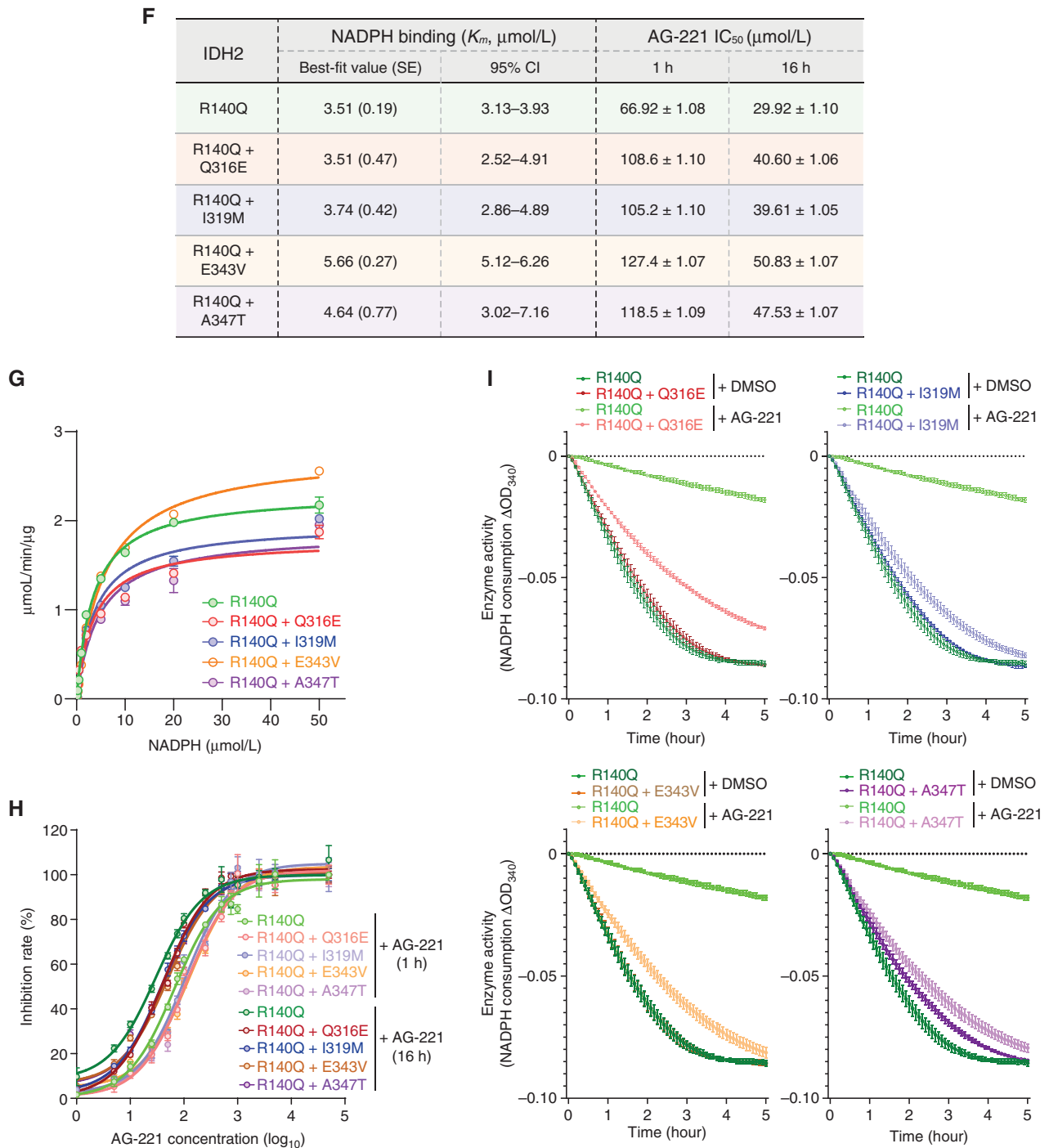


Figure 5. (Continued) F, NADPH binding affinity (K_m) and inhibition potency (IC_{50}) of AG-221 to $\text{IDH2}^{\text{R140Q}}$ alone or with second-site mutations at the dimer interface or NADPH binding sites. Consistent with the mechanism of action, K_m measurements were performed using $\text{IDH2}^{\text{WT}/\text{mut}}$ heterodimers in the presence of NADPH and αKG . The best-fit values \pm SE and 95% confidence interval (CI) are shown. IC_{50} measurements were performed using $\text{IDH2}^{\text{WT}/\text{mut}}$ heterodimers in the presence of NADPH and NADP^+ cofactors after 1 or 16 hours of preincubation and initiated with the addition of αKG . Results are mean \pm SD ($N = 3$ independent measurements). **G**, NADPH binding affinity (K_m) was determined by *in vitro* enzyme assays using IDH2 heterodimers containing R140Q alone or with the indicated second-site mutation. **H**, Inhibition potency of AG-221 (IC_{50} curves) of IDH2 heterodimers containing R140Q alone or with the indicated second-site mutation was determined at 1 or 16 hours. The assay values with AG-221 at 50 $\mu\text{mol/L}$ maximum concentration were scaled to 100%. **I**, IDH2 second-site mutations restored the catalytic activity of $\text{IDH2}^{\text{WT}/\text{R140Q}}$ heterodimers upon AG-221 treatment. NADPH consumption was measured using purified $\text{IDH2}^{\text{WT}/\text{R140Q}}$ heterodimers alone or with second-site mutation in the presence of DMSO or AG-221. Results are mean \pm SD ($N = 3$ independent measurements).

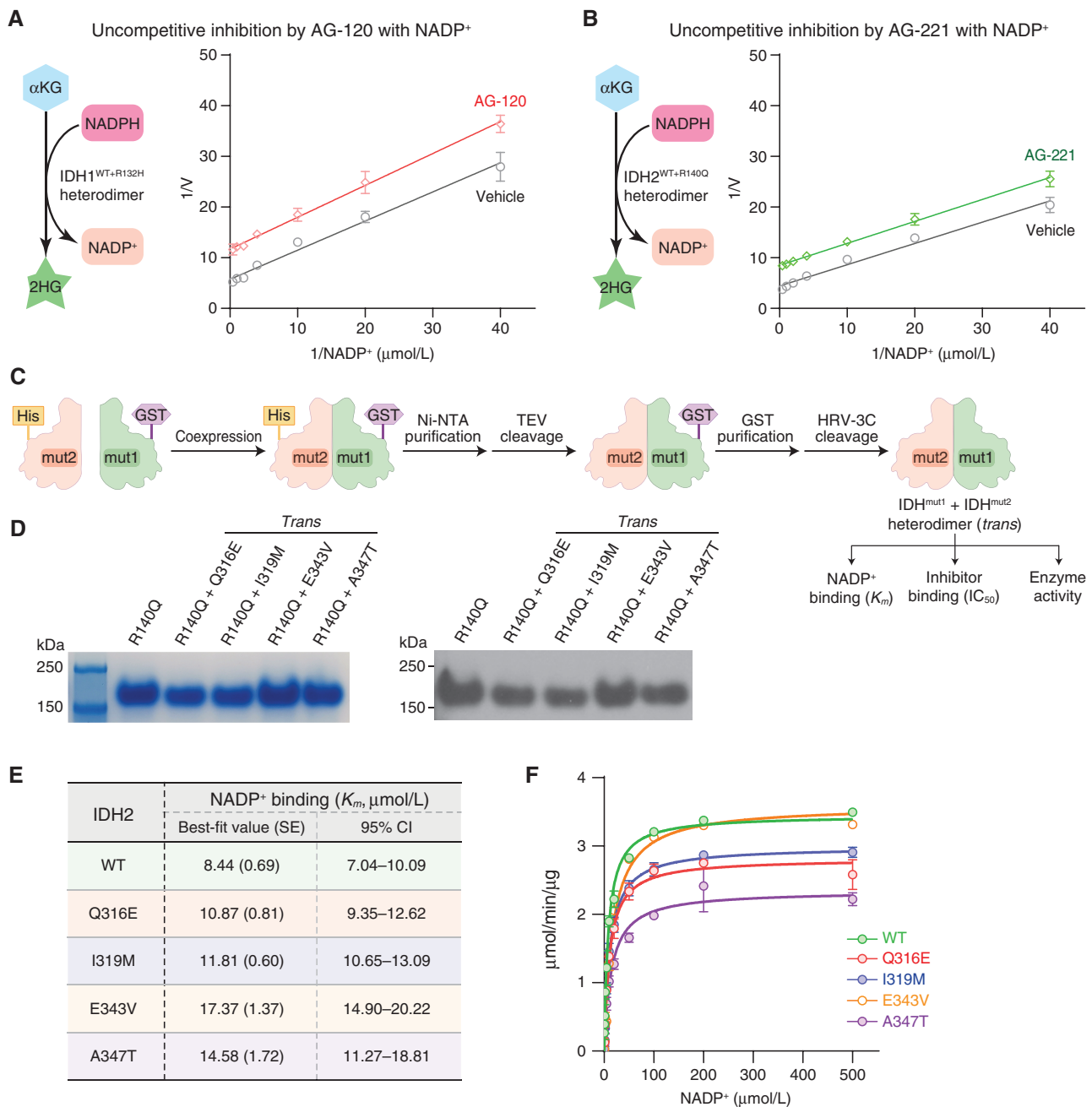


Figure 6. IDH second-site mutations drive acquire resistance by acting in *trans*. **A** and **B**, AG-120 and AG-221 are uncompetitive inhibitors of IDH^{WT/mut} heterodimers with respect to NADP⁺. Linear regression fits of the reciprocal plots for titration series of NADP⁺ versus fixed concentrations of inhibitor yielded parallel lines for both IDH1^{WT/R132H}-AG-120 (**A**) and IDH2^{WT/R140Q}-AG-221 (**B**) complexes. **C**, Schematic of the purification and biochemical analysis of IDH^{mut1} + IDH^{mut2} heterodimers with second-site mutations acting in *trans*. **D**, Validation of purified IDH2^{R140Q} + IDH2^{mut2} heterodimers. IDH2 heterodimers containing R140Q alone or with second-site mutation were analyzed by Western blot. **E** and **F**, NADP⁺ binding affinity (K_m ; **E**) was determined by *in vitro* enzyme assays (**F**) using IDH2 homodimers containing R140Q alone or with the indicated second-site mutations. CI, confidence interval. (continued on following page)

IDH2^{R140Q} + IDH2^{A347T} heterodimers relative to IDH2^{R140Q} alone, resulting in restored IDH2^{R140Q} activity upon AG-221 treatment (Fig. 6G–I). IDH1^{T313I} or IDH1^{H315D} in the context of IDH1^{R132H} also decreased NADP⁺ and inhibitor binding, causing restored enzyme activity in the presence of AG-120 (Supplementary Fig. S8A–S8F). Lastly, we used differential scanning fluorimetry (DSF) to assess the effect of IDH2^{A347T} on AG-221 binding to

the purified IDH2^{R140Q} heterodimers. In line with the enzymology results, the IDH2^{A347T} second-site mutation, located either in *cis* or *trans*, markedly weakened AG-221 binding to IDH2^{mut} enzymes relative to IDH2^{R140Q} alone (Supplementary Fig. S9A–S9C). Hence, second-site mutations can act in *cis* through disabling NADPH-dependent uncompetitive inhibition or in *trans* through disabling NADP⁺-dependent uncompetitive inhibition

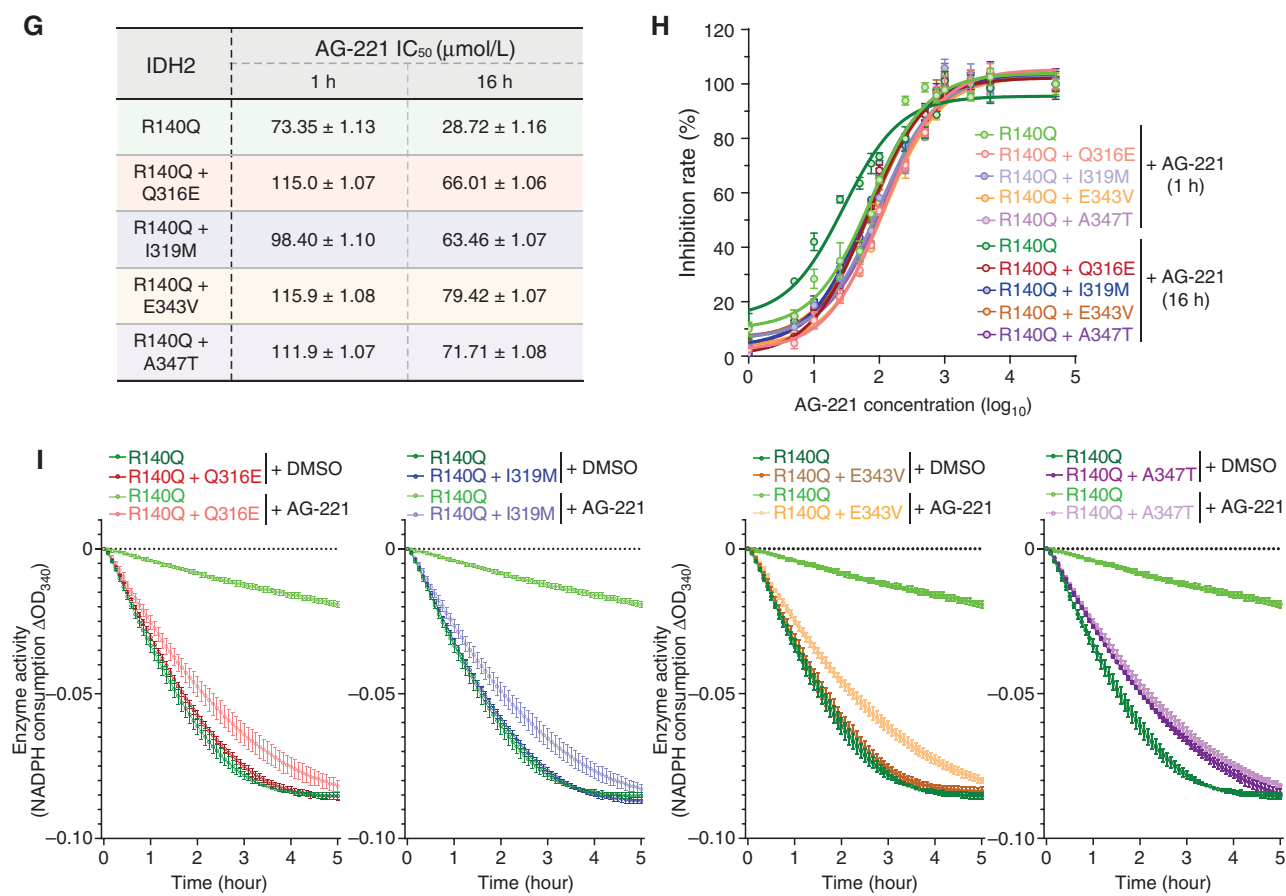


Figure 6. (Continued) **G** and **H**, Inhibition potency (IC₅₀; **G**) and curves (**H**) of AG-221 for IDH2 heterodimers containing R140Q alone or with second-site mutations were determined at 1 or 16 hours. The assay values with AG-221 at 50 μmol/L maximum concentration were scaled to 100%. **I**, IDH2 second-site mutations restored the catalytic activity of IDH2^{WT} + IDH2^{R140Q} heterodimers upon AG-221 treatment. NADPH consumption was measured using purified R140Q heterodimers alone or with second-site mutations at the dimer interface (Q316E and I319M; left) or NADPH binding sites (E343V and A347T; right) in the presence of DMSO or AG-221. Results are mean ± SD (N = 3 independent measurements).

of IDH^{WT/mut} heterodimers, resulting in restored *R*-2HG production to promote therapy resistance to IDH inhibition.

Collectively, by generating clinically relevant IDH^{mut} base-edited leukemia cells and mutagenesis screens of IDH second-site mutations at single amino acid resolution, we uncovered new mechanisms for acquired resistance to IDH inhibition by disabling uncompetitive enzyme inhibition. IDH^{mut} inhibitors AG-120 and AG-221 are slow-tight binders of the dimer interface on IDH1^{mut} and IDH2^{mut} enzymes, respectively. The formation of the IDH^{mut}-inhibitor complex stabilizes the inactive open conformation, prevents conformational change, and blocks IDH^{mut}-catalyzed *R*-2HG production (Fig. 7, models 1 and 2; Supplementary Movies S1 and S2). More importantly, AG-120 and AG-221 are NADPH- and NADP⁺-dependent uncompetitive inhibitors of IDH^{WT/mut} heterodimers. Second-site mutations at NADPH binding sites act in *cis* or *trans* to prevent the formation of stable enzyme-inhibitor complexes, restore mutant IDH enzyme activity in the presence of inhibitors, and drive acquired resistance to IDH inhibition (Fig. 7, models 3 and 4; Supplementary Movies S3 and S4). Hence, our findings not only identify a new class of pathogenic mutations responsible for resistance to IDH inhibition but also establish previously

unrecognized mechanisms for acquired resistance to targeted cancer therapies.

DISCUSSION

Isogenic Cell Models for Studying Mutant IDH-Induced Biological Effects

Therapy resistance to allosteric IDH^{mut} inhibitors emerges as a new challenge; however, due to the lack of preclinical cell models harboring cancer-associated IDH mutations, the mutational repertoire and the underlying mechanisms responsible for acquired resistance to IDH inhibition have remained incompletely understood. The development of sustainable cell lines containing endogenous IDH mutations has been difficult (37). As such, prior functional and biochemical studies were conducted by overexpressing mutant IDH1 or IDH2 in cells harboring wild-type IDH genes (20–22). Hence, establishing clinically relevant cell models with monoallelic IDH mutations is a prerequisite to dissect the biological events involved in tumorigenesis and therapy response.

Here, we used CRISPR base editing to generate a panel of isogenic cell models harboring monoallelic IDH1 or IDH2 oncogenic mutations commonly found in human cancers and

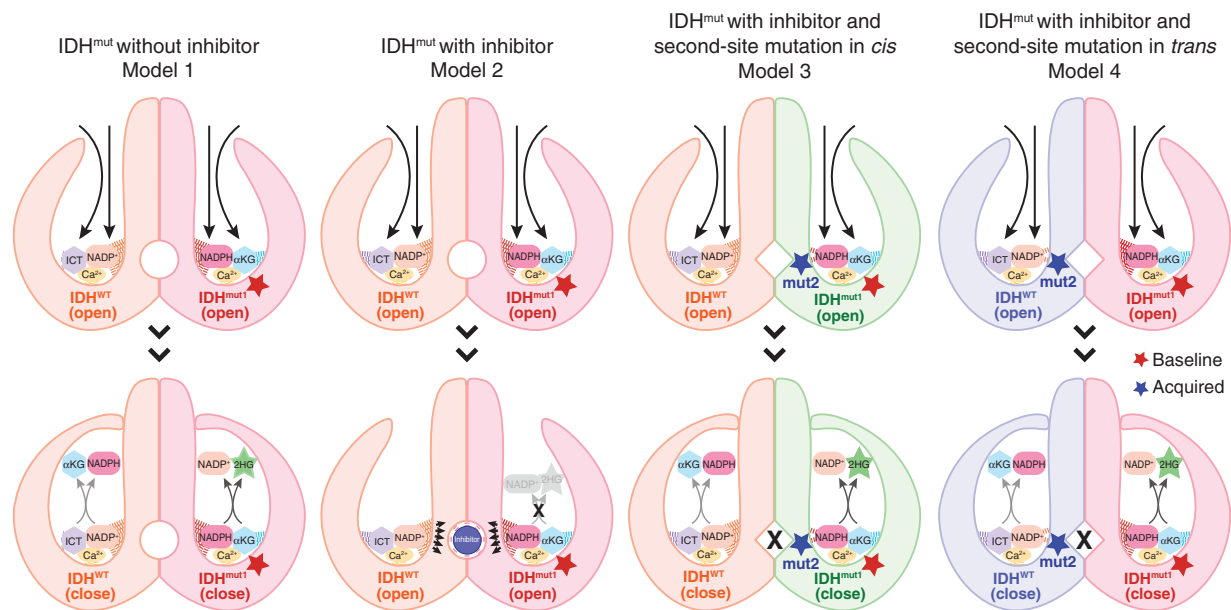


Figure 7. Models of acquired resistance by disabling uncompetitive inhibition. WT IDH enzymes (IDH^{WT}) convert ICT to α KG and generate NADPH, whereas IDH mutations (IDH^{mut1}) reduce α KG to R-2HG and convert NADPH to NADP⁺. IDH^{mut}-catalyzed R-2HG production associates with the change from the inactive open conformation to the close conformation (model 1). AG-120 and AG-221 are slow-tight binders of the dimer interface on IDH1^{R132H} and IDH2^{R140Q}. The formation of the IDH^{mut}-inhibitor complex stabilizes the inactive open conformation and prevents conformational change to block IDH^{mut}-catalyzed R-2HG production (model 2). Acquired second-site mutations (IDH^{mut2}) at NADPH binding sites act in *cis* or *trans* to disable NADPH- or NADP⁺-dependent uncompetitive inhibition of IDH^{WT/mut} heterodimers, prevent the formation of stable enzyme-inhibitor complexes, restore mutant IDH activity in the presence of inhibitors, and drive resistance to IDH inhibition (models 3 and 4).

validated the molecular and functional effects of base-edited IDH mutations in cell and mouse models. The isogenic IDH^{mut} cells recapitulating the naturally occurring IDH mutations will provide valuable models for investigating IDH^{mut}-driven biological events. Using these models, we identified amino acid substitutions conferring resistance to IDH inhibition through saturation variant screens. By integrating these results with targeted sequencing of AML samples and functional studies, we uncovered new mechanisms for acquired resistance by disabling uncompetitive enzyme inhibition. It is important to note that, although our studies were performed in the context of myeloid leukemia, the integrative approaches and reagents should be generally applicable to other IDH^{mut} malignancies, including gliomas, intrahepatic cholangiocarcinomas, and chondrosarcoma, in which IDH inhibitors are being evaluated as targeted therapies (33, 38). Therefore, the development of base-edited cell models and the discovery of second-site mutations associated with acquired resistance will likely have broad implications for understanding the molecular basis of therapy resistance to IDH inhibition in human cancers.

Therapy Resistance Caused by Disabling Uncompetitive Inhibition

Acquired resistance to targeted cancer therapies can arise through distinct mechanisms. Resistance to kinase inhibitors often involves second-site mutations that modulate drug binding or copy-number alterations of the mutated kinases (39–43). In IDH^{mut} malignancies, recurrent second-site mutations at the IDH dimer interface confer resistance by interfering with allosteric inhibitor binding (15). Isoform-switching

mutations also contribute to resistance by restoring R-2HG production (16). Additional mechanisms involving the selection of non-IDH mutations or clonal evolution may contribute to primary or acquired resistance to IDH inhibition by restoring differentiation arrest (17–19, 44).

IDH^{mut} inhibitors ivosidenib (AG-120) and enasidenib (AG-221) represent a new class of cancer therapy due to their unique biochemical features (12, 33). Instead of competitively binding to enzyme active sites, they bind to allosteric sites enclosed within the dimer interface of IDH^{mut} homo- or heterodimers. Consequently, the mutant enzyme adopts an inactive open conformation that is incapable of catalyzing α KG to R-2HG conversion. As such, IDH^{mut} inhibitors show noncompetitive inhibition for α KG but uncompetitive inhibition against IDH^{mut} homo- and heterodimers for NADPH and NADP⁺ cofactors, respectively (ref. 12; Figs. 5A–C and 6A and B).

The mode of uncompetitive inhibition posits that IDH^{mut} inhibitors bind only to the IDH^{mut}-NADPH complex formed between the enzyme and the cofactor (Fig. 5A). Importantly, IDH^{mut} tumor cells have limited availability of NADPH due to the catalytic activity of IDH^{mut} enzymes (Fig. 4E and F; ref. 4). Inhibition of IDH^{mut} restores the NADPH level to facilitate the formation of IDH^{mut}-NADPH-inhibitor complexes due to uncompetitive inhibition. As such, acquired second-site mutations that decrease NADPH binding, such as the mutations identified here, may prevent the formation of stable IDH^{mut}-NADPH-inhibitor complexes without compromising IDH^{mut}-catalyzed α KG reduction to R-2HG (Fig. 7). Hence, tumor cells that acquire recurrent mutations at NADPH binding sites may be positively selected by inhibitor treatment to drive

clonal evolution and therapy resistance. It is important to note that, whereas our studies focused on $IDH^{WT/mut}$ heterodimers, the mechanism of disabling uncompetitive inhibition may also be relevant to IDH^{mut} homodimers to promote acquired resistance to IDH inhibition. In addition, we noted that the VAFs of the second-site mutations are often lower than the primary mutations. Unlike the primary mutations acquired early during clonal evolution, the second-site mutations are likely acquired or selected in subclones. Consistent with this notion, we observed progressively increased VAFs in the longitudinal samples. It is also plausible that the R-2HG–restoring mutations may drive drug resistance in subclones by exporting R-2HG to affect other cells without acquired mutations.

Implications for Understanding Resistance to Targeted Cancer Therapies

Uncompetitive inhibition contributes to various biological processes under physiologic and pathologic conditions. For instance, removing membrane lipids decreases the α -helix content in mitochondria, leading to changes in ATPase that resemble uncompetitive inhibition (45). The N-methyl-D-aspartate receptor (NMDAR) binds glutamate and glycine to control ion transport in response to amino acid binding in neurons. Various blockers have been developed to modify NMDAR activity such as the uncompetitive inhibitor memantine used to treat Alzheimer disease (46).

Here we describe a new class of pathogenic mutations and establish an example that uncompetitive enzyme inhibition can be subverted as a mechanism to drive therapy resistance in human cancers. Through acquisition of secondary mutations to disable uncompetitive inhibition, IDH^{mut} tumors leverage the specific metabolic rewiring to escape allosteric inhibition, restore mutant enzyme activity, and promote therapy resistance. Furthermore, our studies highlight the importance of thorough cataloging of drug-resistance mutations in clinically relevant cell models for developing improved therapies for IDH^{mut} cancers, as exemplified by the development of second- and third-generation inhibitors of BCR–ABL, EGFR, and ALK, or the identification of rational combination therapies (47). The comprehensive identification of second-site mutations with acquired resistance to IDH inhibition enables further investigation of candidate mutations and associated mechanisms, leading to new strategies for monitoring disease progression and preventing or overcoming resistance to targeted cancer therapies.

METHODS

Patient Samples

Selected clot section specimens of bone marrow biopsy used in this study were obtained from relapsed or refractory AML patients positive for $IDH1$ or $IDH2$ mutation after AG-120 or AG-221 treatment with written informed consent in accordance with the Declaration of Helsinki. The collection of these samples was approved by the Institutional Review Board (IRB) of the University of Texas Southwestern Medical Center (UTSW; IRB STU 122013-023 and IRB STU 2019-0815). We analyzed a cohort of 24 AML cases by the following selection criteria: harboring $IDH1$ or $IDH2$ baseline mutation associated with R-2HG production; treated with IDH inhibitor and achieved partial or complete response; relapsed and/or developed resistance to IDH inhibition; and both diagnosis (pretreatment) and posttreatment samples are available for the analysis of IDH mutations.

Mice

NSG-SGM3 (NSGS) transgenic mice expressing human IL3, GM-CSF (CSF2), and SCF (29) were obtained from The Jackson Laboratory (stock no. 013062). Both male and female mice were used unless otherwise specified. All mice were housed under a 12-hour light–dark cycle, 75°F, and 35% humidity in the Animal Resource Center at UTSW. All mouse experiments were performed under protocols approved by the Institutional Animal Care and Use Committee of UTSW.

Cells and Cell Culture

Human TF-1 cells (ATCC, CRL-2003) were cultured in RPMI 1640 medium supplemented with 2 ng/mL recombinant human GM-CSF (PeproTech, 300-03). TF-1 cells with different IDH mutations were cultured without GM-CSF. Human K562 and MOLM-13 cells were cultured in RPMI 1640 medium. HEK293T cells were cultured in DMEM. To generate single cell–derived clones, FACS-sorted cells were plated in 96-well plates and screened by genotyping using targeted sequencing to identify IDH heterozygous mutations. All cell lines were cultured in the medium containing 10% FBS and 1% penicillin/streptomycin at 37°C with 5% CO₂. AG-120 (ApexBio, B7805), AG-881 (Selleck Chemicals, S8611), IDH -305 (MedChem Express, HY-104036), and BAY-1436032 (MedChem Express, HY-100020) were used to treat cells with $IDH1^{R132H}$ mutation alone or with secondary mutations. AG-221 (ApexBio, B7804) and AG-881 were used to treat cells with $IDH2^{R140Q}$ mutation alone or with secondary mutations. All cell lines used in this study tested negative for *Mycoplasma* contamination. No cell line used in this study was found in the database of commonly misidentified cell lines that is maintained by the International Cell Line Authentication Committee and the National Center for Biotechnology Information BioSample.

Plasmids

The luciferase cassette was cloned into the XbaI site of the pLVX-EF1 α -IRES-mCherry vector (Clontech, 631987) using the In-Fusion HD Cloning Kit (Takara Bio, 638911). To generate pLVX-EF1 α -IRES-TagBFP vector, the sequences of IRES and TagBFP were first fused by In-Fusion cloning. The IRES-zsGreen1 cassette of pLVX-EF1 α -IRES-zsGreen1 vector (Clontech, 631982) was then replaced with IRES-TagBFP sequence by In-Fusion cloning. $IDH1^{WT}$ or $IDH2^{WT}$ sequence was cloned to the EcoRI and BamHI sites of the pLVX-EF1 α -IRES-zsGreen1 and pLVX-EF1 α -IRES-TagBFP vectors, respectively. $IDH1^{R132H}$, $IDH2^{R140Q}$, $IDH2^{R140W}$, and $IDH2^{R172K}$ mutations were generated by the Q5 Site-Directed Mutagenesis Kit (New England Biolabs, E0552S) following the manufacturer's instructions and using the pLVX-EF1 α - $IDH1^{WT}$ -IRES-zsGreen1 and pLVX-EF1 α - $IDH2^{WT}$ -IRES-zsGreen1 vectors as templates. Second-site mutations at $IDH1$ or $IDH2$ were generated using pLVX-EF1 α - $IDH1^{R132H}$ -IRES-zsGreen1 and pLVX-EF1 α - $IDH2^{R140Q}$ -IRES-zsGreen1 as the templates, respectively. $IDH1^{WT}$, $IDH2^{WT}$, $IDH1^{R132H}$, and $IDH2^{R140Q}$ sequences were amplified and cloned to BamHI and XhoI sites of pGEX-4T-1 vector (Sigma-Aldrich, GE28-9545-49). $IDH1$ or $IDH2$ sequences with primary or second-site mutations were amplified and cloned to BamHI and HindIII sites of pET28a vector (EMD Biosciences) with an N-terminal 6xHis-SUMO tag. Primers used for cloning and generating the primary or second-site mutations are listed in Supplementary Table S9.

Generation of IDH^{mut} Leukemia Cells by CRISPR Base Editing

We used the optimized CRISPR base-editing method (25) to generate hotspot mutations including $IDH1^{R132H}$ (CGT to CAT), $IDH2^{R140Q}$ (CGG to CAA), $IDH2^{R140W}$ (CGG to TGG), and $IDH2^{R172K}$ (AGG to AAA) in TF-1, K562, and MOLM-13 human leukemia cells, respectively. The CRISPR–Cas9 base editor (Cas9-BE; Addgene, 110869) contains BE3^{RA} [Cas9n with codon optimization and deletion of

premature poly(A) sites], cytidine deaminase APOBEC, UGI domain, and two nuclear-localization signal sequences at the N- or C-terminus. sgRNAs were designed to target individual hotspot mutations in *IDH1* or *IDH2* and cloned into a pSLQ1651 vector (Addgene, 100549) with mCherry. Leukemia cells were transduced with lentiviruses expressing Cas9-BE and sgRNA for each mutation, which were packaged in HEK293T cells as previously described (48), and sorted for EGFP and mCherry-positive cells. Genomic DNA (gDNA) was extracted from single cell-derived clones and used for targeted sequencing. Raw fastq files were mapped to *IDH1* or *IDH2* reference sequences using Bowtie2 with default parameters (49). Mapped reads were extracted from mapping files and aligned together. For each position of piled reads, the counts of bases (A, T, C, and G) and corresponding mutation frequencies for each position were calculated. The mutation frequencies at the base-edited sites in single cell-derived clones (two independent clones for each mutation) are shown in Supplementary Fig. S1B. The sequences for sgRNAs and primers are listed in Supplementary Table S9.

EPO-Induced Cell Differentiation

Parental and base-edited TF-1 cells were induced for erythroid differentiation by EPO as previously described (23, 50). Briefly, cells were washed four times with RPMI 1640 without serum and starved overnight in a medium containing 10% FBS lacking of GM-CSF. Recombinant human EPO (Syd Labs, BP000180-CYT-201) was added to a final concentration of 2 U/mL. After 8 days of induction, erythroid differentiation was assessed by FACS analysis of HbF expression. For intracellular staining of HbF, cells were fixed with 0.05% glutaraldehyde (grade II, Sigma-Aldrich, G6257) for 10 minutes at room temperature and centrifuged for 5 minutes at 600 × g. After permeabilization with 0.1% Triton X-100 in PBS with 0.1% BSA for 5 minutes at room temperature and centrifugation at 600 × g for 15 minutes, cells were incubated with APC-conjugated anti-human HbF antibody (Invitrogen, MHFH05) at 4°C for 20 minutes. Unbound antibodies were washed out using PBS supplemented with 2% FBS. Cells were analyzed using a FACSAria or FACSCanto flow cytometer with the FACSDiva v.8.0.2 software (BD Biosciences).

Inhibitor Selection Screens

Inhibitor selection screens were performed to identify enriched second-site mutations at *IDH1* or *IDH2* that restored R-2HG production in the presence of IDH^{mut} inhibitor AG-120 or AG-221, respectively. We reasoned that if the second-site mutations conferred resistance to IDH^{mut} inhibitor, R-2HG production would be restored to block EPO-induced erythroid differentiation. As such, the second-site mutations would be progressively enriched in HbF-negative undifferentiated cell populations. Base-edited cells were treated with IDH^{mut} inhibitor (AG-120 for *IDH1*^{R132H}-BE cells and AG-221 for *IDH2*^{R140Q}-BE cells) at 1 μmol/L continuously for 16 weeks. EPO at 2 U/mL was then added to induce erythroid differentiation. Cells were stained for HbF expression, and HbF-negative cells were FACS-sorted. gDNA was extracted, and the exon sequences of *IDH1* and *IDH2* genes were PCR-amplified using primers listed in Supplementary Table S9. The DNA fragments for each exon were purified with QIAquick spin columns (Qiagen, 28106), mixed at equal molarity (500 nmol/L), and fragmented to 200 bp using Covaris acoustic shearing following the manufacturer's instructions. Sonicated DNA (25 μL) was processed for library generation using NEBNext Ultra II DNA Kits (New England Biolabs, E7645L) following the manufacturer's protocol. Libraries with different index sequences were quantified, pooled, and sequenced on an Illumina NextSeq 500 system using the 75-bp high-output sequencing kit. Sequencing fastq files were aligned to *IDH1* or *IDH2* reference sequences using BWA mem with default parameters. Reads that are supplementary aligned or not primary aligned were removed using SAMtools (51). SAMtools mpileup was used to generate pileup files from mapping files. pileup2base

(<https://github.com/riverlee/pileup2base>) was used to parse SAMtools pileup file and to obtain the counts of bases (A, T, C, and G) for each position. Mutation frequencies at each position were then calculated from the pileup2base output. The mutation with the highest enrichment at each site is shown in Fig. 2B, and the other enriched mutations at the same site are listed in Supplementary Tables S3 and S8.

Saturation Variant Screens

Saturation variant screens were performed to identify all possible *IDH2* second-site mutations that conferred resistance to AG-221 inhibition. The *IDH2* saturation variant library was designed as described previously (52–55) by substituting each wild-type amino acid at position 41 to 452 (excluding mitochondrial localization signal at positions 1–40 and stop codon at position 453) with one of the other 19 possible amino acids. The saturation variant library was designed and synthesized by Twist Bioscience. Total 7,828 *IDH2*-mutant cDNAs containing a single amino acid substitution were designed and 7,742 mutant cDNAs were confirmed to pass the quality control (Supplementary Table S4). The library containing *IDH2*-mutant alleles was cloned into pLVX-EF1α-IRES-TagBFP vector by Gibson assembly (New England Biolabs, E2611S) following the manufacturer's protocol. The Gibson assembly reaction (1 μL) was electroporated to 25 μL of *E. coli* 10G ELITE SUPREME Electro-competent cells (Lucigen, 60080-2) using a Bio-Rad MicroPulser (Bio-Rad Laboratories). The transformation product was plated onto prewarmed 24.5 cm² bioassay plates with ampicillin. The colonies on the plates were counted to calculate library coverage (>200×). All colonies were collected from the plates and maxiprep was performed to isolate the saturation variant library. Lentiviruses were produced as described previously (48). *IDH2*^{R140Q}-BE cells were transduced with the saturation variant library at low MOI (≤ 0.3) such that the majority of cells received only one mutant allele. Over 5 × 10⁶ BFP⁺ cells were FACS-sorted to get enough coverage of each mutant allele (>500×). Cells were collected before AG-221 treatment as the baseline time point (T0) and then treated with AG-221 at 1 μmol/L for the selection of second-site mutations associated with drug resistance. After 2, 4, 6, 8, and 10 weeks (T1 to T5) following AG-221 treatment, cells were induced for erythroid differentiation by EPO for 8 days and HbF-negative cells were FACS-sorted. gDNA was isolated, and *IDH2* cDNA sequences were PCR-amplified using Phusion High-Fidelity DNA Polymerase (New England Biolabs, M0530L) with the primers listed in Supplementary Table S9. DNA fragments were diluted to 1 ng/μL and fragmented to 200 bp using Covaris acoustic shearing following the manufacturer's instructions. Twenty-five microliters of sonicated DNA were processed for library generation. Libraries with different index sequences were sequenced on an Illumina NextSeq 500 system using the 75-bp high-output sequencing kit. Initial data processing and alignment were performed by ORFCall (<https://github.com/tedsharpe/ORFCall>). ORFCall aligns reads to the *IDH2* reference sequence. The counts for all 64 possible codons at each codon position were tallied and normalized by total codon counts. Codon enrichment was then calculated as the ratio of normalized codon counts between different time points (T1–T5) and T0. The mutations with progressive enrichment from T1 to T5 were selected by MaSigPro (56). The mutation with the highest enrichment at each site is shown in Fig. 2D, and the other enriched mutations enriched at the same site are listed in Supplementary Table S5.

Targeted Sequencing of IDH Genes in Patient Samples

Targeted sequencing of *IDH1* and *IDH2* genes was performed using bone marrow specimens from matched diagnosis and relapsed AML patients with *IDH* baseline mutation before or after IDH^{mut} inhibitor treatment. gDNA was extracted from the bone marrow clot sections using the QuickExtract FFPE DNA extraction kit (Epicenter

Biotechnologies, QEF81805) following the manufacturer's instructions. For each sample, the exon sequences of *IDH1* and *IDH2* genes were PCR-amplified using primers located in the intronic regions and purified with QIAquick spin columns. Library preparation, sequencing, and data analysis were performed as described in the inhibitor selection screens.

Analysis of Cis or Trans Configuration of IDH Primary and Secondary Mutations

Allele-specific amplicon sequencing was performed to identify the *cis* or *trans* configuration of the primary and secondary mutations in patients UT8, MDA2, and MDA7. Specifically, gDNA from these samples was isolated and used for targeted sequencing. Primers were designed to amplify the genomic region spanning exons 4 and 8 of *IDH2*. The 3.6-kb PCR products were cloned into EcoRI and BamHI sites of the pLVX-EF1 α -IRES-zsGreen1 vector using the In-Fusion HD Cloning Kit. After transformation and verification by colony PCR and real-time PCR, the plasmid DNA was isolated and used for Sanger sequencing. For the analysis of *cis* or *trans* configuration in leukemia cells, the base-edited cells from inhibitor selection screens were collected to isolate RNA by TRIzol (Life Technologies, 15596018). cDNA was generated using an iScript DNA synthesis kit (Bio-Rad, 1708891) following the manufacturer's instructions and used for PCR cloning of *IDH1* or *IDH2* regions containing the primary and secondary mutations. Amplicon libraries with different index sequences were quantified and pooled, followed by paired-end sequencing on an Illumina NextSeq 500 system. Sequencing reads were aligned to the WT or mutant reference sequences and counted. The numbers and percentages of reads with mutations identified in *cis* or *trans* are listed in Supplementary Table S7. The primers used for cloning and sequencing are listed in Supplementary Table S9.

R-2HG Measurement

R-2HG was measured by LC/MS or the assay kit (BioVision, K213-100) following the manufacturer's instructions. Intracellular R-2HG was quantified in cell pellets from 2×10^6 cells. For R-2HG measurement in culture medium, 200 μ L medium was mixed with 800 μ L methanol and dried with a SpeedVac into a pellet. The dried pellet was resuspended in 100 μ L of freshly mixed 80:20 acetonitrile:acetic acid solution with 50 mg/mL diacetyl-L-tartaric anhydride (DATAN, Sigma-Aldrich, 358924) and $U^{13}C$ D/L-2HG solution (Cambridge Isotope Laboratories, CLM-10351-0.001) as internal standards. After sonication and heating at 75°C for 30 minutes, samples were cooled to room temperature and centrifuged. The resulting supernatant was dried with a SpeedVac to a pellet. The pellet was reconstituted in 100 μ L of 1.5 mmol/L ammonium formate aqueous solution with 10% acetonitrile. LC/MS analysis of R-2HG levels was performed on an AB Sciex 5500 QTRAP liquid chromatography/mass spectrometer (Applied Biosystems SCIEX) and analyzed by the AB Sciex Analyst 1.6.1 Software as previously described (57). Waters Acquity UPLC HSS T3 column (150 \times 2.1 mmol/L, 1.8 μ mol/L) was operated at 35°C for separation. Different 2-hydroxyglutarate-diacetyl tartrate derivatives, 363/147 (CE: -14 V) and 368/152 (internal standard, CE: -14 V), were checked with multiple reaction monitoring.

NADPH and NADP⁺ Measurement

NADPH and NADP⁺ levels in unmodified TF-1 cells or TF-1 cells stably expressing primary and/or second-site IDH mutations were measured using the NADP/NADPH Glo-Assay (Promega, G9081; refs. 58, 59) following the manufacturer's instructions. After the standard curves were generated using the purified NADPH (Sigma-Aldrich, N7505) and NADP⁺ (Sigma-Aldrich, N5755) in the same buffer as the experimental samples, the absolute amount of NADPH and NADP⁺ was obtained for each sample.

NADPH Oxidation Analysis

NADPH oxidation analysis was performed as previously described (4, 15). Specifically, cells were collected and cleaved by M-PER lysis buffer (Thermo Scientific, 78503) supplemented with protease and phosphatase inhibitors (Sigma-Aldrich, PPC1010). After centrifugation at 21,000 \times g for 10 minutes, the supernatant was collected, quantified by BCA assay (Thermo Scientific, PI-23225), and normalized by total protein concentration. Purified proteins were also quantified by BCA assay for measuring enzymatic activity. Three micrograms of cell lysates or purified proteins were added to 200 μ L of assay buffer containing 33 mmol/L Tris-acetate (pH 7.4, NovaTeinBio, NBB-2410), 1.3 mmol/L MgCl₂, 25 μ mol/L β -NADPH, 40 mmol/L NaHCO₃, and 0.6 mmol/L α KG (Sigma-Aldrich, 75890), and absorbance at 340 nm was measured every minute for 5 hours. Datapoints were averaged among 5 time points centered at every 5 minutes and represented by the mean activity of 3 replicates.

Xenograft Experiments

TF-1 cells with stable luciferase expression were generated as previously described (60). Briefly, cells were transduced with lentiviruses produced with the pLVX-EF1 α -Luc2-IRES-mCherry vector and mCherry-positive cells were FACS-sorted. Cells were then transduced with lentiviruses expressing *IDH*^{WT} with BFP and *IDH*^{mut1} or *IDH*^{mut1+mut2} with zsGreen1, and FACS-sorted. Eight- to 10-week-old NSGS mice were intravenously transplanted with mCherry, BFP, and zsGreen1 triple-positive cells (1×10^6 per mice) resuspended in PBS (200 μ L per mice). Following intraperitoneal injection of D-Luciferin (Gold Biotechnology, LUCK-1G) at 150 mg/kg, bioluminescence imaging was performed 4 hours after transplant to confirm fluorescent signals and ensure successful transplantation procedures. After disease onset for 7 days, the engrafted mice were randomly assigned for treatment with vehicle solution (control) or 30 mg/kg of AG-120 or AG-221 as described previously (12). When the mice became moribund after treatment with vehicle or inhibitors for 28 days, bioluminescence imaging was performed and intensity was quantitated by the Living Image v.3.2 acquisition and analysis software (Caliper Life Science). Total flux values were determined by regions of interest with an identical size for each mouse and presented in photons per second (p/s). Leukemia cell frequencies in peripheral blood and bone marrow were monitored by flow cytometry as previously described (61).

Expression and Purification of IDH Heterodimers

IDH^{WT/R132H} and IDH^{WT/R140Q} heterodimers were generated by cotransformation of plasmids containing GST-tagged *IDH*^{WT} and 6xHis-tagged *IDH*^{mut1} into *E. coli* Rosetta2 (DE3) cells. For IDH^{WT} + IDH^{mut1+mut2} heterodimers with second-site mutations in *cis*, plasmids containing GST-tagged *IDH*^{WT} and 6xHis-tagged *IDH*^{mut1+mut2} were cotransformed. For IDH^{mut1} + IDH^{mut2} heterodimers with second-site mutations in *trans*, plasmids containing GST-tagged *IDH*^{mut1} and 6xHis-tagged *IDH*^{mut2} were cotransformed. Cells were selected with ampicillin and kanamycin. Protein expression and purification were performed as described previously (62). Specifically, *E. coli* Rosetta 2 (DE3) cells cotransformed with *IDH*-expressing plasmids were grown in LB medium with antibiotics at 37°C until OD₆₀₀ reached 0.6 to 0.8. Then, 0.5 mmol/L isopropyl- β -D-thiogalactoside (IPTG) was added to induce protein expression at 18°C overnight. After centrifugation at 4,000 \times g for 10 minutes at 4°C, cell pellets were resuspended in buffer containing 300 mmol/L NaCl, 50 mmol/L Tris-HCl pH 8.0, 10% glycerol, 2 mmol/L β -mercaptoethanol (β ME), and 1 mmol/L PMSF and were lysed by sonication. The supernatant was collected by centrifugation at 12,000 \times g for 10 minutes at 4°C and flowed through Ni-NTA resin (G-Biosciences, 786-940) five times for the binding of 6xHis-tagged proteins. After washing with buffer 1 (20 mmol/L imidazole, 1 M NaCl, 50 mmol/L Tris-HCl pH 8.0, 10% glycerol, and 2 mmol/L

β ME) and buffer 2 (20 mmol/L imidazole, 100 mmol/L NaCl, 50 mmol/L Tris-HCl pH 8.0, 10% glycerol, and 2 mmol/L β ME), proteins were eluted with buffer 3 (250 mmol/L imidazole, 100 mmol/L NaCl, 50 mmol/L Tris-HCl pH 8.0, 5% glycerol, and 2 mmol/L β ME). The eluate was incubated with TEV protease at 4°C overnight followed by incubation with GST resin (Thermo Scientific, 16101) for 2 hours at 4°C with mixing. After washing with buffer 1 (0.1% NP40, 500 mmol/L NaCl, 50 mmol/L Tris-HCl pH 8.0, 10% glycerol, and 2 mmol/L DTT), buffer 2 (1 M NaCl, 50 mmol/L Tris-HCl pH 8.0, 10% glycerol, and 2 mmol/L DTT), and buffer 3 (100 mmol/L NaCl, 50 mmol/L Tris-HCl pH 8.0, 10% glycerol, and 2 mmol/L DTT), protein-bound GST resin was incubated with HRV-3C protease at 4°C overnight. The flow-through fractions were collected by eluting with buffer 4 (100 mmol/L NaCl, 20 mmol/L Tris-HCl pH 8.0, and 2 mmol/L DTT). The proteins were quantified by BCA assay and stored as aliquots at -80°C .

Native PAGE and Western Blot Analysis

Different IDH heterodimers isolated with tandem affinity purification were validated by native polyacrylamide gel electrophoresis (PAGE), followed by Coomassie blue staining and Western blot. The purified proteins were quantified by a BCA assay. Protein samples were prepared with native sample buffer (Bio-Rad, 1610738) and separated on a PAGE gel with nonreducing buffer in the absence of SDS. The proteins on the gel were stained with Colloidal Blue Staining Kit (Thermo Scientific, LC6025) following the manufacturer's instructions or transferred to Amersham Hybond P 0.45 PVDF blots (GE HealthCare, 10600023). After blocking with 5% nonfat milk in TBST (20 mmol/L Tris-HCl pH 7.5, 150 mmol/L NaCl, and 0.1% Tween-20), the blots were incubated with antibodies against IDH1 (Proteintech, 12332-1-AP) or IDH2 (Abcam, ab55271) with 1:500 dilution at 4°C overnight with shaking, followed by secondary antibodies at room temperature for 1 hour. The blots were washed with TBST three times before and after antibody incubation and developed with Plus-ECL (PerkinElmer, NEL104001EA). To measure histone methylation, Western blot analysis was performed as previously described (63) with antibodies against H3K4me3 (Abcam, ab8580), H3K9me2 (Abcam, ab1220), H3K9me3 (Abcam, ab8898), H3K27me3 (Millipore Sigma, 07-449), H3K36me3 (Abcam, ab9050), H3K79me2 (Abcam, ab3594), and total H3 (Abcam, ab1791) with 1:1,000 dilution.

Uncompetitive Inhibition of IDH^{mut} Inhibitors

For uncompetitive inhibition by AG-120 and AG-221 with regard to NADPH, IDH1^{WT+R132H} and IDH2^{WT+R140Q} heterodimer proteins were diluted to 100 nmol/L in 120 μL assay buffer (20 mmol/L Tris pH 7.5, 150 mmol/L NaCl, 10 mmol/L MgCl_2 , 10% glycerol, and 0.03% BSA) containing vehicle or IDH^{mut} inhibitor (100 nmol/L AG-120 for IDH1^{WT+R132H} or 75 nmol/L AG-221 for IDH2^{WT+R140Q}), 1 $\mu\text{mol/L}$ NADP⁺, and NADPH dilution series. For uncompetitive inhibition by AG-120 and AG-221 with regard to NADP⁺, heterodimer proteins were diluted to 50 nmol/L in 120 μL assay buffer (20 mmol/L Tris pH 7.5, 150 mmol/L NaCl, 10 mmol/L MgCl_2 , 10% glycerol, and 0.03% BSA) containing vehicle or IDH^{mut} inhibitor (1 $\mu\text{mol/L}$ AG-120 for IDH1^{WT+R132H} or 25 $\mu\text{mol/L}$ AG-221 for IDH2^{WT+R140Q}), 10 $\mu\text{mol/L}$ NADPH, and NADP⁺ dilution series. After 1-hour incubation at 25°C to allow the formation of complexes containing inhibitor, IDH heterodimer, NADP⁺, and NADPH, the reaction was initiated by adding 30 μL assay buffer with 6.25 mmol/L αKG , incubated for 2 minutes at 25°C, and terminated by adding 50 μL assay buffer with 36 $\mu\text{g/mL}$ of diaphorase and 18 $\mu\text{mol/L}$ resazurin. The remaining NADPH levels were measured on a FLUOstar Omega plate reader (BMG Labtech) via fluorescence ($\lambda_{\text{ex}} = 544 \text{ nm}$, $\lambda_{\text{em}} = 590 \text{ nm}$). Three independent measurements were performed for each dilution of NADPH or NADP⁺. The curves were generated in GraphPad Prism software.

Analysis of NADPH and NADP⁺ Binding Affinity

Analysis of binding affinity between NADPH and IDH heterodimers or NADP⁺ and IDH homodimers with or without second-site mutations was performed as previously described (4, 12). Briefly, to determine the binding affinity of NADPH to heterodimers with or without second-site mutations, 20 to 100 nmol/L of purified proteins were diluted in the assay buffer (20 mmol/L Tris pH 7.5, 150 mmol/L NaCl, 10 mmol/L MgCl_2 , 10% glycerol, and 0.03% BSA) with NADPH dilution series. The reactions were initiated by adding 6.25 mmol/L αKG in the assay buffer. After incubation for 10 minutes at room temperature, the reactions were then terminated by adding assay buffer with 36 $\mu\text{g/mL}$ of diaphorase and 18 $\mu\text{mol/L}$ resazurin, and mixed for 1 minute with a shaker. The remaining NADPH levels were measured on a plate reader by fluorescence ($\lambda_{\text{ex}} = 544 \text{ nm}$, $\lambda_{\text{em}} = 590 \text{ nm}$). To determine the binding affinity of NADP⁺ to homodimers with first- and/or second-site mutations, 1 to 5 $\mu\text{mol/L}$ purified proteins were diluted in the assay buffer with NADP⁺ dilution series. The reactions were initiated by adding assay buffer with 0.2 mmol/L ICT, 60 $\mu\text{g/mL}$ diaphorase, and 200 $\mu\text{mol/L}$ resazurin. After running for 30 minutes at room temperature, the reactions were terminated by adding 6% SDS with mixing for 1 minute. NADPH generated by the reactions was measured on a plate reader. Absolute NADPH concentration for each sample was obtained using an NADPH standard curve generated in the assay buffer alone. Three independent measurements were performed for each dilution of NADPH or NADP⁺. The curve, best-fit values \pm SE, and 95% confidence interval of K_m for each sample were generated in GraphPad Prism.

Analysis of Inhibitor IC₅₀

IDH heterodimer proteins with or without second-site mutations were diluted to 0.25 $\mu\text{g/mL}$ in 120 μL assay buffer (20 mmol/L Tris pH 7.5, 150 mmol/L NaCl, 10 mmol/L MgCl_2 , 10% glycerol, and 0.06% BSA) containing IDH^{mut} inhibitor dilution series, 42.5 $\mu\text{mol/L}$ NADP⁺, 5 $\mu\text{mol/L}$ NADPH, and 2.5 mmol/L β ME. The mixture was incubated at 25°C for 1 hour or 16 hours. The reaction was initiated by adding 30 μL assay buffer with 6.25 mmol/L αKG . The reactions were run for 50 minutes at 25°C and terminated by 50 μL assay buffer with 36 $\mu\text{g/mL}$ of diaphorase and 18 $\mu\text{mol/L}$ resazurin. After shaking the reaction for 1 minute, the NADPH levels were measured on a plate reader by fluorescence ($\lambda_{\text{ex}} = 544 \text{ nm}$, $\lambda_{\text{em}} = 590 \text{ nm}$). Three replicates were performed for each dilution of IDH^{mut} inhibitors. The assay values with AG-120 or AG-221 at 50 $\mu\text{mol/L}$ maximum concentration were scaled to 100%. The curve and value of IC₅₀ for each sample were generated in GraphPad Prism.

Structural Modeling

Structural analysis was performed based on the crystal structures of 20a (an AG-120 analogue)-bound IDH1 (PDB #5L57) and AG-221-bound IDH2 (PDB #5I96; refs. 12, 28). Structure figures were rendered in PyMOL Molecular Graphics System (Version 1.2r3pre; Schrödinger, LLC). The biologically relevant IDH1 dimer was constructed by combining the deposited structure of one protomer with the structure of another symmetry-related protomer. Point mutations were generated in Coot (64), and mutated residues were represented as rotamers with the highest probability that do not sterically clash with other residues in the structure.

DSF

IDH2^{R140Q} proteins with or without second-site mutations at 1 $\mu\text{mol/L}$ concentration were mixed with 50 $\mu\text{mol/L}$ NADP⁺, 5 $\mu\text{mol/L}$ NADPH, and the indicated concentrations of AG-221 (Cayman, 21277) in 20 μL assay buffer (20 mmol/L Tris pH 7.5, 150 mmol/L NaCl, 10 mmol/L MgCl_2 , and 2% DMSO). The mixtures were

incubated at 25°C for 16 hours before adding SYPRO orange (Sigma, S5692) with a 1,000-fold dilution of the stock. The dye-containing mixtures were transferred to a 96-well plate to acquire fluorescence signals at temperatures ranging from 20°C to 85°C on a Roche LightCycler480 real-time PCR machine. T_m values corresponding to the maxima of the negative first derivative of fluorescence signals as a function of temperature were manually recorded. The apparent K_d values were determined using GraphPad Prism.

Quantification and Statistical Analysis

Statistical details including N , mean, and statistical significance values are indicated in the text, figure legends, or methods. Error bars in the experiments represent SEM, SE, or SD from either independent experiments or independent samples. All statistical analyses were performed using GraphPad Prism software unless otherwise specified, and the detailed information about statistical methods is specified in figure legends or methods. The numbers of independent experiments or biological replicate samples and P values (*, $P < 0.05$; **, $P < 0.01$; ***, $P < 0.001$; ****, $P < 0.0001$; n.s., not significant) are provided in individual figures. $P < 0.05$ was considered statistically significant. Figures 5E and 6D and Supplementary Figs. S1C, S7A, and S8A show a representative image at least three independent experiments or biological replicate samples with similar results.

Data and Software Availability

All processed datasets for targeted sequencing and screens are available in Supplementary Tables S2–S6. Raw sequencing data are deposited in the European Nucleotide Archive under accession number PRJEB48042. Targeted sequencing analyses were performed using Bowtie2 v2.2.8, BWA v0.7.17, SAMtools v 0.1.19, pileup2base (<https://github.com/riverlee/pileup2base>), MaSigPro, and ORFCall (<https://github.com/tedsharpe/ORFCall>). Code for analyses using other indicated software is available from the websites of the corresponding software.

Authors' Disclosures

Y.F. Madanat reports other support from Blueprint Medicines, GERON, OncLive, Sierra Oncology, Stemline Therapeutics, Novartis, and Morphosys outside the submitted work. P. Patel reports other support from Servier and Bristol Myers Squibb/Celgene outside the submitted work, and is an employee of Servier BioInnovation but was at the University of Texas Southwestern at the time of this work. A.S. Mims reports other support from The Leukemia & Lymphoma Society, personal fees from Servier Pharmaceuticals, Syndax Pharmaceuticals, Astellas Pharmaceuticals, Jazz Pharmaceuticals, Daiichi Sanyo, Bristol Myers Squibb, Ryvu Therapeutics, Genentech, and AbbVie outside the submitted work. U. Borate reports grants and personal fees from Bristol Myers Squibb and AbbVie outside the submitted work. S.F. Cai reports other support from Imago Biosciences outside the submitted work. R.J. DeBerardinis reports personal fees from Agios Pharmaceuticals outside the submitted work. J. Xu reports grants from the NIH, the Cancer Prevention & Research Institute of Texas, The Leukemia & Lymphoma Society, the American Society of Hematology, and the Welch Foundation during the conduct of the study. No disclosures were reported by the other authors.

Authors' Contributions

J. Lyu: Conceptualization, data curation, formal analysis, validation, investigation, methodology, writing—original draft, writing—review and editing. **Y. Liu:** Data curation, software, formal analysis, methodology. **L. Gong:** Data curation, formal analysis, investigation, methodology. **M. Chen:** Resources, data curation, methodology. **Y.F. Madanat:** Resources, methodology. **Y. Zhang:** Data curation, software, formal analysis, methodology. **F. Cai:** Formal analysis, investigation, methodology. **Z. Gu:** Investigation, methodology.

H. Cao: Investigation, project administration. **P. Kaphle:** Investigation. **Y.J. Kim:** Investigation. **F.N. Kalkan:** Resources, methodology. **H. Stephens:** Resources, methodology. **K.E. Dickerson:** Methodology. **M. Ni:** Resources, software, investigation, methodology. **W. Chen:** Resources, data curation. **P. Patel:** Resources, methodology. **A.S. Mims:** Resources, methodology. **U. Borate:** Resources, methodology. **A. Burd:** Resources, methodology. **S.F. Cai:** Resources, data curation, methodology. **C.C. Yin:** Resources, data curation, methodology. **M.J. You:** Resources, data curation. **S.S. Chung:** Resources, supervision, methodology, project administration. **R.H. Collins:** Resources, supervision, project administration. **R.J. DeBerardinis:** Resources, supervision, funding acquisition. **X. Liu:** Software, formal analysis, supervision, funding acquisition, investigation, methodology, writing—original draft. **J. Xu:** Conceptualization, resources, supervision, funding acquisition, methodology, writing—original draft, project administration, writing—review and editing.

Acknowledgments

We are grateful to Ralf Kittler, Paul Yenerall, and Rahul Kollipara for helping with data analysis and discussions; Ryan Huang for assay design; Ashley Yocum and Timothy Chen for assistance with Beat AML samples; and other Xu laboratory members for technical support. J. Xu is a Scholar of The Leukemia & Lymphoma Society and an American Society of Hematology Scholar. This work was supported by NIH grants R01DK111430, R01CA230631, R01CA259581, and R21AI158240 to J. Xu; NIH grants R01GM121662 and R01GM136308 to X. Liu; Cancer Prevention & Research Institute of Texas grants RP180504, RP190417, RP220337, and RP220375 (to J. Xu); and Welch Foundation grants (I-1942 to J. Xu and I-1790 to X. Liu).

The publication costs of this article were defrayed in part by the payment of publication fees. Therefore, and solely to indicate this fact, this article is hereby marked “advertisement” in accordance with 18 USC section 1734.

Note

Supplementary data for this article are available at Cancer Discovery Online (<http://cancerdiscovery.aacrjournals.org/>).

Received December 19, 2021; revised August 31, 2022; accepted October 4, 2022; published first October 12, 2022.

REFERENCES

- Parsons DW, Jones S, Zhang X, Lin JC, Leary RJ, Angenendt P, et al. An integrated genomic analysis of human glioblastoma multiforme. *Science* 2008;321:1807–12.
- Yan H, Parsons DW, Jin G, McLendon R, Rasheed BA, Yuan W, et al. IDH1 and IDH2 mutations in gliomas. *N Engl J Med* 2009;360:765–73.
- Mardis ER, Ding L, Dooling DJ, Larson DE, McLellan MD, Chen K, et al. Recurring mutations found by sequencing an acute myeloid leukemia genome. *N Engl J Med* 2009;361:1058–66.
- Dang L, White DW, Gross S, Bennett BD, Bittinger MA, Driggers EM, et al. Cancer-associated IDH1 mutations produce 2-hydroxyglutarate. *Nature* 2009;462:739–44.
- Ward PS, Patel J, Wise DR, Abdel-Wahab O, Bennett BD, Collier HA, et al. The common feature of leukemia-associated IDH1 and IDH2 mutations is a neomorphic enzyme activity converting alpha-ketoglutarate to 2-hydroxyglutarate. *Cancer Cell* 2010;17:225–34.
- Gross S, Cairns RA, Minden MD, Driggers EM, Bittinger MA, Jang HG, et al. Cancer-associated metabolite 2-hydroxyglutarate accumulates in acute myelogenous leukemia with isocitrate dehydrogenase 1 and 2 mutations. *J Exp Med* 2010;207:339–44.
- Figuroa ME, Abdel-Wahab O, Lu C, Ward PS, Patel J, Shih A, et al. Leukemic IDH1 and IDH2 mutations result in a hypermethylation phenotype, disrupt TET2 function, and impair hematopoietic differentiation. *Cancer Cell* 2010;18:553–67.

8. Xu W, Yang H, Liu Y, Yang Y, Wang P, Kim SH, et al. Oncometabolite 2-hydroxyglutarate is a competitive inhibitor of α -ketoglutarate-dependent dioxygenases. *Cancer Cell* 2011;19:17–30.
9. Lu C, Ward PS, Kapoor GS, Rohle D, Turcan S, Abdel-Wahab O, et al. IDH mutation impairs histone demethylation and results in a block to cell differentiation. *Nature* 2012;483:474–8.
10. Saha SK, Parachoniak CA, Ghanta KS, Fitamant J, Ross KN, Najem MS, et al. Mutant IDH inhibits HNF-4 α to block hepatocyte differentiation and promote biliary cancer. *Nature* 2014;513:110–4.
11. Stein EM, DiNardo CD, Pollyea DA, Fathi AT, Roboz GJ, Altman JK, et al. Enasidenib in mutant IDH2 relapsed or refractory acute myeloid leukemia. *Blood* 2017;130:722–31.
12. Yen K, Travins J, Wang F, David MD, Artin E, Straley K, et al. AG-221, a first-in-class therapy targeting acute myeloid leukemia harboring oncogenic IDH2 mutations. *Cancer Discov* 2017;7:478–93.
13. DiNardo CD, Stein EM, de Botton S, Roboz GJ, Altman JK, Mims AS, et al. Durable remissions with ivosidenib in IDH1-mutated relapsed or refractory AML. *N Engl J Med* 2018;378:2386–98.
14. Hopkins AL, Groom CR. The druggable genome. *Nat Rev Drug Discovery* 2002;1:727–30.
15. Intlekofer AM, Shih AH, Wang B, Nazir A, Rustenburg AS, Albanese SK, et al. Acquired resistance to IDH inhibition through trans or cis dimer-interface mutations. *Nature* 2018;559:125–9.
16. Harding JJ, Lowery MA, Shih AH, Schwartzman JM, Hou S, Famulare C, et al. Isoform switching as a mechanism of acquired resistance to mutant isocitrate dehydrogenase inhibition. *Cancer Discov* 2018;8:1540–7.
17. Choe S, Wang H, DiNardo CD, Stein EM, de Botton S, Roboz GJ, et al. Molecular mechanisms mediating relapse following ivosidenib monotherapy in IDH1-mutant relapsed or refractory AML. *Blood Advances* 2020;4:1894–905.
18. Wang F, Morita K, DiNardo CD, Furudate K, Tanaka T, Yan Y, et al. Leukemia stemness and co-occurring mutations drive resistance to IDH inhibitors in acute myeloid leukemia. *Nat Commun* 2021;12:2607.
19. Quek L, David MD, Kennedy A, Metzner M, Amatangelo M, Shih A, et al. Clonal heterogeneity of acute myeloid leukemia treated with the IDH2 inhibitor enasidenib. *Nat Med* 2018;24:1167–77.
20. Zhao S, Lin Y, Xu W, Jiang W, Zha Z, Wang P, et al. Glioma-derived mutations in IDH1 dominantly inhibit IDH1 catalytic activity and induce HIF-1 α . *Science* 2009;324:261–5.
21. Rohle D, Popovici-Muller J, Palaskas N, Turcan S, Grommes C, Campos C, et al. An inhibitor of mutant IDH1 delays growth and promotes differentiation of glioma cells. *Science* 2013;340:626–30.
22. Wang F, Travins J, DeLaBarre B, Penard-Lacronique V, Schalm S, Hansen E, et al. Targeted inhibition of mutant IDH2 in leukemia cells induces cellular differentiation. *Science* 2013;340:622–6.
23. Losman JA, Looper RE, Koivunen P, Lee S, Schneider RK, McMahon C, et al. (R)-2-hydroxyglutarate is sufficient to promote leukemogenesis and its effects are reversible. *Science* 2013;339:1621–5.
24. Komor AC, Kim YB, Packer MS, Zuris JA, Liu DR. Programmable editing of a target base in genomic DNA without double-stranded DNA cleavage. *Nature* 2016;533:420–4.
25. Zafra MP, Schatoff EM, Katti A, Foronda M, Breinig M, Schweitzer AY, et al. Optimized base editors enable efficient editing in cells, organoids and mice. *Nat Biotechnol* 2018;36:888–93.
26. Sasaki M, Knobbe CB, Munger JC, Lind EF, Brenner D, Brustle A, et al. IDH1(R132H) mutation increases murine haematopoietic progenitors and alters epigenetics. *Nature* 2012;488:656–9.
27. Papaemmanuil E, Gerstung M, Bullinger L, Gaidzik VI, Paschka P, Roberts ND, et al. Genomic classification and prognosis in acute myeloid leukemia. *N Engl J Med* 2016;374:2209–21.
28. Jones S, Ahmet J, Ayton K, Ball M, Cockerill M, Fairweather E, et al. Discovery and optimization of allosteric inhibitors of mutant isocitrate dehydrogenase 1 (R132H IDH1) displaying activity in human acute myeloid leukemia cells. *J Med Chem* 2016;59:11120–37.
29. Wunderlich M, Chou FS, Link KA, Mizukawa B, Perry RL, Carroll M, et al. AML xenograft efficiency is significantly improved in NOD/SCID-IL2RG mice constitutively expressing human SCF, GM-CSF and IL-3. *Leukemia* 2010;24:1785–8.
30. Konteatis Z, Artin E, Nicolay B, Straley K, Padyana AK, Jin L, et al. Vorasidenib (AG-881): a first-in-class, brain-penetrant dual inhibitor of mutant IDH1 and 2 for treatment of glioma. *ACS Med Chem Lett* 2020;11:101–7.
31. Cho YS, Levell JR, Liu G, Caferro T, Sutton J, Shafer CM, et al. Discovery and evaluation of clinical candidate IDH305, a brain penetrant mutant IDH1 inhibitor. *ACS Med Chem Lett* 2017;8:1116–21.
32. Pusch S, Krausert S, Fischer V, Balss J, Ott M, Schrimpf D, et al. Pan-mutant IDH1 inhibitor BAY 1436032 for effective treatment of IDH1 mutant astrocytoma in vivo. *Acta Neuropathol* 2017;133:629–44.
33. Popovici-Muller J, Lemieux RM, Artin E, Saunders JO, Salituro FG, Travins J, et al. Discovery of AG-120 (ivosidenib): a first-in-class mutant IDH1 inhibitor for the treatment of IDH1 mutant cancers. *ACS Med Chem Lett* 2018;9:300–5.
34. Yang B, Zhong C, Peng Y, Lai Z, Ding J. Molecular mechanisms of “off-on switch” of activities of human IDH1 by tumor-associated mutation R132H. *Cell Res* 2010;20:1188–200.
35. Pietrak B, Zhao H, Qi H, Quinn C, Gao E, Boyer JG, et al. A tale of two subunits: how the neomorphic R132H IDH1 mutation enhances production of α HG. *Biochemistry* 2011;50:4804–12.
36. Holdgate GA, Meek TD, Grimley RL. Mechanistic enzymology in drug discovery: a fresh perspective. *Nat Rev Drug Discovery* 2018;17:115–32.
37. Piaskowski S, Bienkowski M, Stoczynska-Fidelus E, Stawski R, Sieruta M, Szybka M, et al. Glioma cells showing IDH1 mutation cannot be propagated in standard cell culture conditions. *Br J Cancer* 2011;104:968–70.
38. Mellinghoff IK, Ellingson BM, Touat M, Maher E, De La Fuente MI, Holdhoff M, et al. Ivosidenib in isocitrate dehydrogenase 1-mutated advanced glioma. *J Clin Oncol* 2020;38:3398–406.
39. Shah NP, Nicoll JM, Nagar B, Gorre ME, Paquette RL, Kuriyan J, et al. Multiple BCR-ABL kinase domain mutations confer polyclonal resistance to the tyrosine kinase inhibitor imatinib (STI571) in chronic phase and blast crisis chronic myeloid leukemia. *Cancer Cell* 2002;2:117–25.
40. Cools J, Mentens N, Furet P, Fabbro D, Clark JJ, Griffin JD, et al. Prediction of resistance to small molecule FLT3 inhibitors: implications for molecularly targeted therapy of acute leukemia. *Cancer Res* 2004;64:6385–9.
41. Kobayashi S, Boggon TJ, Dayaram T, Jänne PA, Kocher O, Meyerson M, et al. EGFR mutation and resistance of non-small-cell lung cancer to gefitinib. *N Engl J Med* 2005;352:786–92.
42. Choi YL, Soda M, Yamashita Y, Ueno T, Takashima J, Nakajima T, et al. EML4-ALK mutations in lung cancer that confer resistance to ALK inhibitors. *N Engl J Med* 2010;363:1734–9.
43. Woyach JA, Furman RR, Liu TM, Ozer HG, Zapatka M, Ruppert AS, et al. Resistance mechanisms for the Bruton’s tyrosine kinase inhibitor ibrutinib. *N Engl J Med* 2014;370:2286–94.
44. Miles LA, Bowman RL, Merlinsky TR, Csete IS, Ooi AT, Durruthy-Durruthy R, et al. Single-cell mutation analysis of clonal evolution in myeloid malignancies. *Nature* 2020;587:477–82.
45. Lenaz G, Curatola G, Mazzanti L, Parenti-Castelli G. Biophysical studies on agents affecting the state of membrane lipids: biochemical and pharmacological implications. *Mol Cell Biochem* 1978;22:3–32.
46. Parsons CG, Stöfler A, Danysz W. Memantine: a NMDA receptor antagonist that improves memory by restoration of homeostasis in the glutamatergic system—too little activation is bad, too much is even worse. *Neuropharmacology* 2007;53:699–723.
47. Cohen P, Cross D, Jänne PA. Kinase drug discovery 20 years after imatinib: progress and future directions. *Nat Rev Drug Discovery* 2021;20:551–69.
48. Liu X, Zhang Y, Chen Y, Li M, Zhou F, Li K, et al. In situ capture of chromatin interactions by biotinylated dCas9. *Cell* 2017;170:1028–43.
49. Langmead B, Salzberg SL. Fast gapped-read alignment with Bowtie 2. *Nat Methods* 2012;9:357–9.
50. Canver MC, Smith EC, Sher F, Pinello L, Sanjana NE, Shalem O, et al. BCL11A enhancer dissection by Cas9-mediated in situ saturating mutagenesis. *Nature* 2015;527:192–7.

51. Li H, Handsaker B, Wysoker A, Fennell T, Ruan J, Homer N, et al. The sequence alignment/map format and SAMtools. *Bioinformatics* 2009;25:2078–9.
52. Boettcher S, Miller PG, Sharma R, McConkey M, Leventhal M, Krivtsov AV, et al. A dominant-negative effect drives selection of TP53 missense mutations in myeloid malignancies. *Science* 2019;365:599–604.
53. Giacomelli AO, Yang X, Lintner RE, McFarland JM, DUBY M, Kim J, et al. Mutational processes shape the landscape of TP53 mutations in human cancer. *Nat Genet* 2018;50:1381–7.
54. Majithia AR, Tsuda B, Agostini M, Gnanapradeepan K, Rice R, Peloso G, et al. Prospective functional classification of all possible missense variants in PPARG. *Nat Genet* 2016;48:1570–5.
55. Melnikov A, Rogov P, Wang L, Gnirke A, Mikkelsen TS. Comprehensive mutational scanning of a kinase in vivo reveals substrate-dependent fitness landscapes. *Nucleic Acids Res* 2014;42:e112.
56. Nueda MJ, Tarazona S, Conesa A. Next maSigPro: updating maSigPro bioconductor package for RNA-seq time series. *Bioinformatics* 2014;30:2598–602.
57. Xiong N, Gao X, Zhao H, Cai F, Zhang FC, Yuan Y, et al. Using arterial-venous analysis to characterize cancer metabolic consumption in patients. *Nat Commun* 2020;11:3169.
58. Piskounova E, Agathocleous M, Murphy MM, Hu Z, Huddleston SE, Zhao Z, et al. Oxidative stress inhibits distant metastasis by human melanoma cells. *Nature* 2015;527:186–91.
59. Tasdogan A, Faubert B, Ramesh V, Ubellacker JM, Shen B, Solmonson A, et al. Metabolic heterogeneity confers differences in melanoma metastatic potential. *Nature* 2020;577:115–20.
60. Li K, Zhang Y, Liu X, Liu Y, Gu Z, Cao H, et al. Noncoding variants connect enhancer dysregulation with nuclear receptor signaling in hematopoietic malignancies. *Cancer Discov* 2020;10:724–45.
61. Gu Z, Liu Y, Zhang Y, Cao H, Lyu J, Wang X, et al. Silencing of LINE-1 retrotransposons is a selective dependency of myeloid leukemia. *Nat Genet* 2021;53:672–82.
62. Chen S, Jiao L, Shubbar M, Yang X, Liu X. Unique structural platforms of Suz12 dictate distinct classes of PRC2 for chromatin binding. *Mol Cell* 2018;69:840–52.
63. Gu Z, Liu Y, Cai F, Patrick M, Zmajkovic J, Cao H, et al. Loss of EZH2 reprograms BCAA metabolism to drive leukemic transformation. *Cancer Discov* 2019;9:1228–47.
64. Emsley P, Lohkamp B, Scott WG, Cowtan K. Features and development of Coot. *Acta Crystallogr D Biol Crystallogr* 2010;66(Pt 4):486–501.